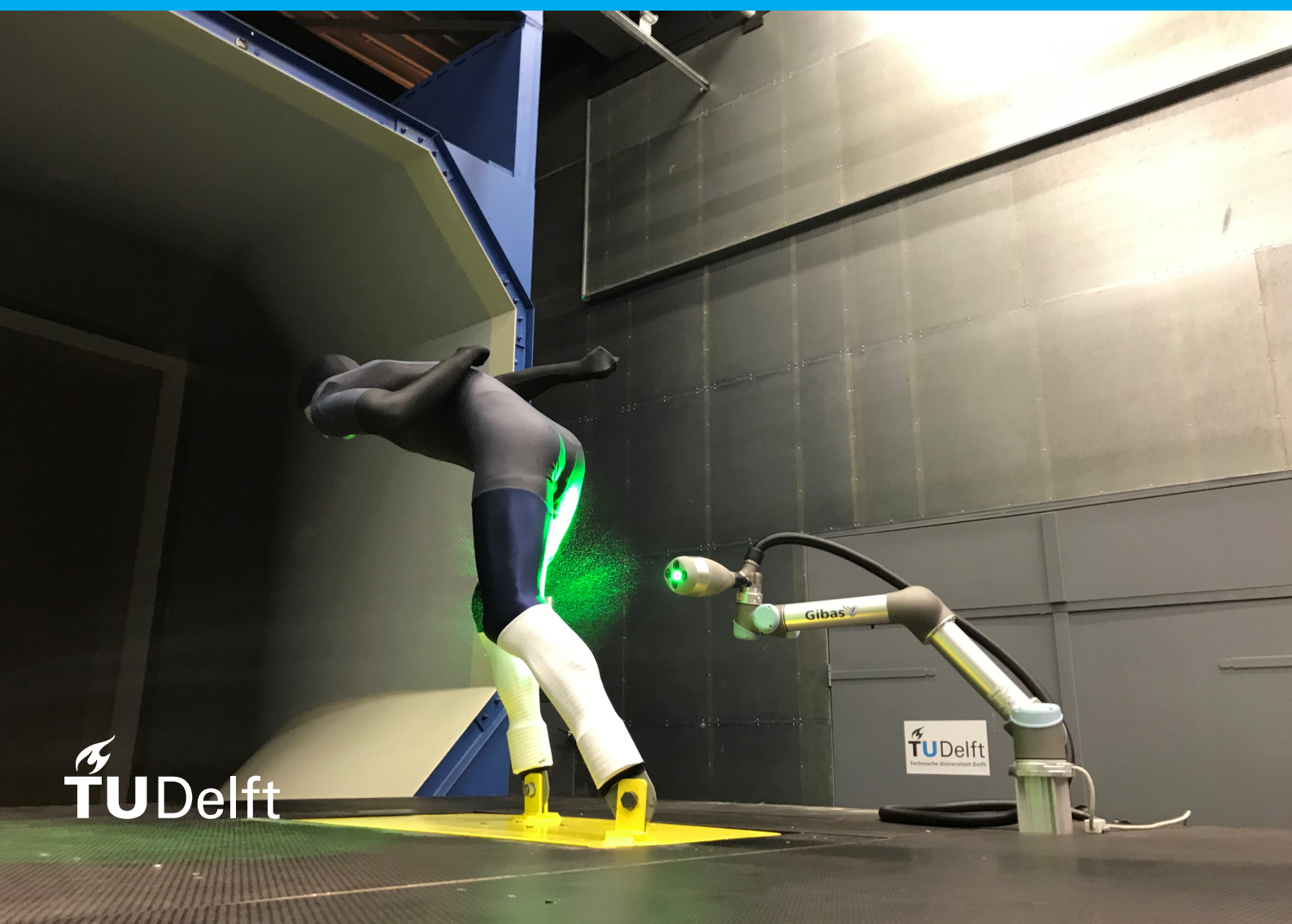


# Aerodynamics of a skater leg

Experimental investigation on Reynolds number effects

J. van Voorden

February 2021



# Aerodynamics of a skater leg

Experimental investigation on Reynolds  
number effects

by

J. van Voorden

to obtain the degree of Master of Science  
at the Delft University of Technology,  
to be defended publicly on Tuesday March 2, 2021 at 10:00 AM.

Student number:	4351460	
Thesis committee:	Prof. dr. Frans C. T. van der Helm,	TU Delft, supervisor
	Dr. Andrea Sciacchitano,	TU Delft, weekly supervisor
	Dr. Wouter Terra,	TU Delft, weekly supervisor
	Ir. W. A. Nando Timmer ,	TU Delft, external member

*This thesis is confidential and cannot be made public until March 1, 2021.*

An electronic version of this thesis is available at <http://repository.tudelft.nl/>.

## **Abstract**

The design of current skating suits is based on the assumption that the flow across the skater body parts is highly similar to cylinder flow. The latter features drag crisis behaviour, resulting in significant drag reduction at the critical Reynolds number. However, whether the aforementioned assumption is valid and whether a drag crisis along the different body parts occurs, so far remains unknown.

The goal of this study is to investigate Reynolds number effects along the leg of a skater mannequin. To do so, potential drag crisis behaviour is studied via robotic Particle Image Velocimetry and Infrared Thermography for speeds ranging between 5 m/s and 25 m/s. The boundary layer state and the critical velocity distribution along the leg, based on the wake width variation, are evaluated for the bare mannequin and the mannequin wearing a skating suit optimized for  $\sim 15$  m/s.

Results reveal drag crisis behaviour along the knee, lower and upper leg. Furthermore, the flow topology is not only governed by the leg geometry, but also by streamwise vortices. These streamwise vortices cause an increase of the wake width below the calf and a reduced velocity deficit behind the upper leg. Most significant differences in wake width between the bare and the dressed leg are observed at 17.5 m/s. The latter observation is also supported by the Infrared Thermography results.

It can be concluded that the flow across the leg partly differs from cylinder flow, mainly because of streamwise vortices that locally affect the drag crisis behaviour.

## Preface

This thesis presents my work on the topic of skating aerodynamics, as partial fulfilment of the requirements for the degree of Master of Science. The idea behind my thesis was initiated in 2019 while attending the two-week course of 'Special Topics in Sports Engineering'. During this course, an internship project related to skating aerodynamics was offered by NOC-NSF. I seized this opportunity with both hands, mainly because of my interests in aerodynamics and because of the fact that I am a fanatic ice skater myself. After finishing my internship, I was eager to find a Master's thesis topic that built on the work of my internship project. Accordingly, together with two of my supervisors Dr. A. Sciacchitano and Dr. W. Terra we discussed the possible thesis topics. This eventually led to the present Master's thesis.

The Master's research provided the opportunity to utilize high-end equipment and facilities. For the latter, I am truly grateful. Moreover, I learned a lot about, among others, setting up an experiment, the utilization of new software and equipment and writing a scientific paper. The aforementioned things could not have been attained without Dr. A. Sciacchitano and Dr. W. Terra who enabled me to start off this project.

I would like to thank Dr. A. Sciacchitano, Dr. W. Terra and Prof. Dr. F. C. T. van der Helm for the contributions to my thesis. In addition, I would like to express my appreciation to Dr. A. Sciacchitano, Dr. W. Terra for all the valuable discussions during the weekly meetings that helped me overcome the different and sometimes difficult obstacles during the project.

I also like to thank the technical staff from the aerodynamics department and in particular Dr. W. Terra for helping me with building the measurement set-up. Furthermore, I would like to thank Ir. Edoardo Saredi and the LaVision Service Team for helping me out with the software related problems in Davis 10, needed to process the data. Moreover, I like to thank Bert van der Tuuk for providing the skating suit and the skating mannequin.

Last but not least, I like to express my gratitude for the support that my parents, friends, family and girlfriend provided throughout the project. Your trust and encouragements helped me to overcome the challenges that I faced.

*J. van Voorden  
Zoetermeer, February 2021*

## Nomenclature

$\Delta T$	Absolute temperature difference	[°C]
$\Delta t_1$	Pulse separation of first acquisition	[s]
$\Delta t_2$	Pulse separation of second acquisition	[s]
$\epsilon_{dw}$	Uncertainty of wake width $d_w$	[m]
$\epsilon_u$	Relative random uncertainty of the time-average velocity	[-]
$\epsilon_{v,crit}$	Uncertainty of critical velocity $v_{crit}$	[m/s]
$\omega_x$	Streamwise vorticity	[s <sup>-1</sup> ]
$\sigma_u$	Standard deviation of the time-average streamwise velocity	[m/s]
$A$	Frontal area	[m <sup>2</sup> ]
$C_d$	Drag coefficient	[-]
$d$	Local leg width	[m]
$d_w$	Local wake width	[m]
$h$	Spacing between adjacent velocity vectors	[m]
$k$	Coverage factor, normal distribution	[-]
$N$	Number of particles inside a bin	[-]
$Re$	Reynolds number	[-]
$Re_{crit}$	Critical Reynolds number	[-]
$U_\infty$	Free-stream velocity	[m/s]
$U_x$	Streamwise velocity	[m/s]
$v_{crit}$	Critical velocity	[m/s]
$x$	Streamwise distance to origin	[m]
$y$	Vertical distance to origin	[m]
$z$	Horizontal distance to origin	[m]

# Contents

<b>1</b>	<b>Introduction</b>	<b>1</b>
<b>2</b>	<b>Methods</b>	<b>3</b>
2.1	Robotic PIV measurements . . . . .	3
2.1.1	Wake width evaluation . . . . .	3
2.2	IT measurements. . . . .	3
<b>3</b>	<b>Experimental set-up</b>	<b>4</b>
3.1	Wind tunnel and skating mannequin. . . . .	4
3.2	Measurement equipment-Robotic PIV. . . . .	5
3.3	Measurement equipment-Infrared Thermography . . . . .	6
3.4	PIV measurement uncertainty . . . . .	6
<b>4</b>	<b>Results</b>	<b>8</b>
4.1	Force balance measurements . . . . .	8
4.2	Global flow characteristics . . . . .	8
4.2.1	Bare mannequin . . . . .	8
4.2.2	Dressed mannequin . . . . .	9
4.3	Reynolds number effects: Comparison between the bare and the dressed leg . . . . .	10
4.3.1	Spanwise non-dimensional velocity profiles at different free-stream velocities . . . . .	10
4.3.2	Local wake width . . . . .	10
4.3.3	Critical velocity . . . . .	12
4.3.4	Optimal suit performance . . . . .	13
4.4	Infrared Thermography. . . . .	14
<b>5</b>	<b>Discussion</b>	<b>16</b>
<b>6</b>	<b>Conclusion</b>	<b>18</b>
<b>A</b>	<b>Infrared Thermography</b>	<b>19</b>
A.1	Physics behind IT. . . . .	19
A.2	The steady active IT technique . . . . .	19
A.3	Practical example. . . . .	20
<b>B</b>	<b>Suit figures</b>	<b>21</b>
<b>C</b>	<b>Particle Image Velocimetry</b>	<b>23</b>
C.1	Tomographic-PIV . . . . .	23
C.2	Robotic volumetric Particle Image Velocimetry . . . . .	23
C.2.1	Tracer particles . . . . .	24
C.2.2	Lagrangian Particle Tracking - Shake-The-Box . . . . .	24
C.2.3	PIV applications in sport aerodynamics . . . . .	25
<b>D</b>	<b>Processing operations in Davis: From raw data to binned particle tracks</b>	<b>27</b>
D.1	Masking function . . . . .	27
D.2	Image pre-processing . . . . .	28
D.3	Shake-The-Box . . . . .	28
D.4	Merging and binning of the particle tracks. . . . .	28
<b>E</b>	<b>Possible time saving</b>	<b>30</b>
	<b>References</b>	<b>31</b>

# 1. Introduction

Skating suits can have a significant impact on the performance of a speed skater since around 80% of the total resistance force of a skater is caused by aerodynamic drag [25]. This, along with the fact that the difference between winning and losing can be determined by a thousandth of a second, made that several researchers have investigated the optimization of the skating suit. It has led to a tight-fitting suit, with among others, optimised fabrics for the different body parts and seams that are strategically positioned on the suit. Many of these improvements have been achieved by performing force balance measurements on cylinders to, for example, evaluate the drag reduction performance of different fabrics [22][21]. This provides insight into which fabric or configuration results in minimal drag, but does not contribute to a better understanding of how the flow around a skater behaves. Enhanced understanding of the flow behaviour around a skater and how this behaviour is affected by local suit properties, may significantly contribute to the improvement of the skating suit design. However, in literature very little is reported about these 3D flow structures around a skater body and about how these are affected by surface properties. A skater is often represented by a combination of multiple bluff bodies, as it is believed that the flow around these bodies shows high similarities with the flow around the different body parts of a skater. Typical examples of bluff bodies are spheres and cylinders. Their aerodynamics have already been thoroughly studied, resulting in extensive knowledge about the effects of: roughness [3][4], local trips [7], shape [23] and the orientation [22][34] on the aerodynamics of bluff bodies. Based on the Reynolds number, the flow across smooth spheres and cylinders can be classified into three different regimes [16]. For Reynolds numbers in the range of  $\sim 10^3 - 2.0 \cdot 10^5$  the flow is in the sub-critical regime, characterized by an early laminar boundary separation, causing a large wake and high-pressure drag. For Reynolds numbers between  $2.0 \cdot 10^5$  and  $5.0 \cdot 10^5$ , the flow is in its critical state, with a region of laminar separation and turbulent reattachment of the flow, known as the separation bubble. This results in the point of separation being relocated significantly further downstream, leading to a narrow wake. Within the critical flow regime around  $Re \sim 3.7 \cdot 10^5$ , the drag crisis occurs, referring to the point where the drag coefficient is at its minimum [8]. The Reynolds number at which minimum drag occurs is referred to as the critical Reynolds number ( $Re_{crit}$ ). The third regime is the super-critical flow state in which the flow becomes fully turbulent before it separates,  $Re > 5.0 \cdot 10^5$ , resulting in an increase of the drag coefficient again.

So, spheres and cylinders experience the least drag force when the so-called drag crisis is encountered. Due to the similarities between human body parts and bluff bodies, the drag crisis is expected to occur also along the body parts of a skater. However, this usually does not occur at the velocities that are attained during a skating race. Nevertheless, a drag crisis at lower velocities can be forced. This generally is achieved by applying roughness to the surface. Sports such as speed skating, downhill-skiing [5] and cycling [6] apply fabrics with a distributed roughness on the suits. Most of the time, these fabrics are first tested on a cylinder in a wind tunnel before applying them to a suit.

Besides the use of cylinders for the performance evaluation of roughened fabrics, mannequins are also used to evaluate the performance of complete suits [21]. Considering the complexity of the body geometry, using a real-sized mannequin is generally seen as a more advanced approach. Next to this, the beneficial effect of applying roughness is usually reduced when there is flow interaction between objects [22]. These effects are not captured when testing on a single cylinder. D’auteuil et al. (2010) even demonstrated that the choice for the optimal fabric was affected by the flow interaction between the body parts [9]. Besides flow interaction, also possible streamwise vortices emanating from the body may locally affect the potential drag crisis behaviour. So, the aforementioned examples again emphasize the high importance of understanding the flow features along the different limbs of a skater, when trying to optimize the suit design. The problem, however, is that it is still unknown whether a drag crisis occurs at the different body parts of skater, and if so at which critical Reynolds number.

To understand these flow features, one may visualize the full three-dimensional flow field around the skater. A measurement technique that enables such quantitative flow visualization is robotic volumetric Particle Image Velocimetry (PIV). Robotic PIV has already shown its high potential within the field of cycling aerodynamics [32]. Also, visualization of the boundary layer state on the body’s surface may

contribute to an enhanced understanding by providing information about, among others, the location of flow separation and the type of boundary layer prior to separation. Infrared thermography (IT) is a measurement technique that enables this type of visualization. Accordingly, Robotic PIV and IT may provide information that is of fundamental importance.

The goal of this study is to investigate the Reynolds number effects along the leg of a skater mannequin and to investigate how these are affected by suit surface properties. This is done by studying the flow around a 1:1 scale skater mannequin, for flow speeds ranging from 5 to 25 m/s, utilizing robotic PIV and IT. The focus will be on the flow around the right leg of the mannequin, which is its standing leg. First, the drag reduction performance of the skating suit is evaluated via force balance measurements. Then, the main flow features of the bare mannequin at typical racing speed are discussed, followed by a comparison with the dressed mannequin. Next, the Reynolds number effects along the leg are discussed. Lastly, the most striking differences between both configurations will be discussed and compared to the observations from the IT measurements.

## 2. Methods

### 2.1. Robotic PIV measurements

The wake flow topology of the skater leg is visualized, utilizing the robotic PIV technique. The flow across the leg is measured at 7 different free-stream velocities;  $U_\infty = 5, 10, 12.5, 15, 17.5, 20, 25$  m/s. Based on a width of 0.1 m for the lower leg, the Reynolds number is in the range of  $3.3 \cdot 10^4$  and  $1.6 \cdot 10^5$ . The flow around the right leg is divided into 5 different cones and is measured for the bare and dressed mannequin. The flow features are captured for both configurations, first of all, to demonstrate the potential effect of the local suit surface properties on the wake flow topology with respect to the bare mannequin. Secondly, most CFD analyses use models without surface roughness. Capturing the flow features of the bare mannequin thus enables validation of potential CFD analyses.

The position of the probe, containing the four cameras and the optical fibre that transmits the laser light, is controlled by the robot arm that is connected to the probe. To capture the flow properties around the leg for the 7 different velocities, the multi- $\Delta t$  3D-PTV approach is selected [26]. The helium filled soap bubbles (HFSB) in the flow are tracked with the Shake-the-Box (STB) double-frame algorithm [29] in Davis 10 from Lavisision GmbH. The multi- $\Delta t$  method uses two different pulse separations. The measurements at  $\Delta t_1$  are used as a predictor;  $\Delta t_1$  is chosen in such a way that the particle displacement in the free-stream between two pulses is approximately 3 mm.  $\Delta t_2$  extends the dynamic velocity range, with a particle displacement of 10 mm between two consecutive pulses. Both  $\Delta t_1$  and  $\Delta t_2$  capture 10,000 images. Eventually, this results in 1,400,000 images ( $7 \times 5 \times 2 \times 2 \times 10,000$ ) in the entire measurement domain, considering the 7 different free-stream velocities.

#### 2.1.1. Wake width evaluation

The critical velocity at which the drag crisis occurs is then determined, based on the free-stream velocity for which the wake width is minimal. To determine these wake widths, the approach of Terra et al. (2020) is adopted [32]. They evaluated the wake width based on the distance between the velocity inflection points, which is equal to the distance between the peaks of  $|\partial U_x / \partial z|$ . The wake widths are evaluated at a distance behind the leg of 1.1 times the leg width and are evaluated between  $y = 215 - 575$  mm, with a spatial resolution of  $\sim 16$  mm. For  $y > 575$  mm, data coverage is not sufficient to determine the wake widths.

### 2.2. IT measurements

While on the one hand, visualization and quantification of the wake flow topology are enabled by robotic PIV, the IT measurement technique, on the other hand, can visualize the location of flow separation on the leg and the boundary layer state prior to the separation. Just as with the PIV measurements, data is recorded at  $U_\infty = 5, 10, 12.5, 15, 17.5, 20, 25$  m/s. For the IT measurements, the active steady technique is employed [27]. With this technique, the leg of the mannequin is first heated from both sides, then the wind tunnel is activated which at the same time cools down the surface. After reaching thermal equilibrium, the steady temperature is measured. Fifty-one images per position are recorded at a frame rate of 32 Hz to capture the steady temperature. Also, while the leg is heated, a zero measurement is performed ( $U_\infty = 0$ ), at the start and end of a full velocity sweep. Eventually, the 51 images for each configuration are averaged and subtracted from the first zero measurement. This results in an absolute temperature difference  $\Delta T$ . High values of  $\Delta T$  indicate regions of high surface cooling, pointing at regions of a turbulent boundary layer. Low values of  $\Delta T$  on the other hand, indicate regions of low cooling, hinting at a laminar boundary layer. Lastly, when flow separation occurs, the heat transfer locally goes to zero, resulting in a  $\Delta T$  of around zero, recognized by the dark blue areas on the leg. More information on the Infrared Thermography measurement technique is provided in appendix A.

### 3. Experimental set-up

#### 3.1. Wind tunnel and skating mannequin

The experiments are performed in the closed-circuit Open Jet Facility (OJF) of the Delft University of Technology. The OJF is a low-speed wind tunnel, that operates up to a speed of 35 m/s. The tunnel has an octagonal cross-section, with a cross-sectional area of  $2.85 \times 2.85 \text{ m}^2$ , the tunnel hall itself has a width and height of 13 and 8 meters respectively. The turbulence intensity of the free-stream flow is measured at around 0.5% [17]. The mannequin used for the experiment features a skater that just performed the side-push motion with its left leg, therefore the left leg is held backwards. For this particular position, the right leg is its stance leg. The 3D model of the mannequin, together with the relevant dimensions can be seen in figure 3.1. The state-of-the-art skating suit that is applied to the mannequin consists of three different fabrics across the leg. The top fabric on the upper leg is a smooth fabric, followed by a fabric containing a distributed roughness pattern that is covering part of the upper leg and the knee. The lower leg is covered with a fabric containing a distributed roughness pattern having a higher roughness than the fabric on part of the upper leg and knee. Figures of the suit are shown in appendix B.

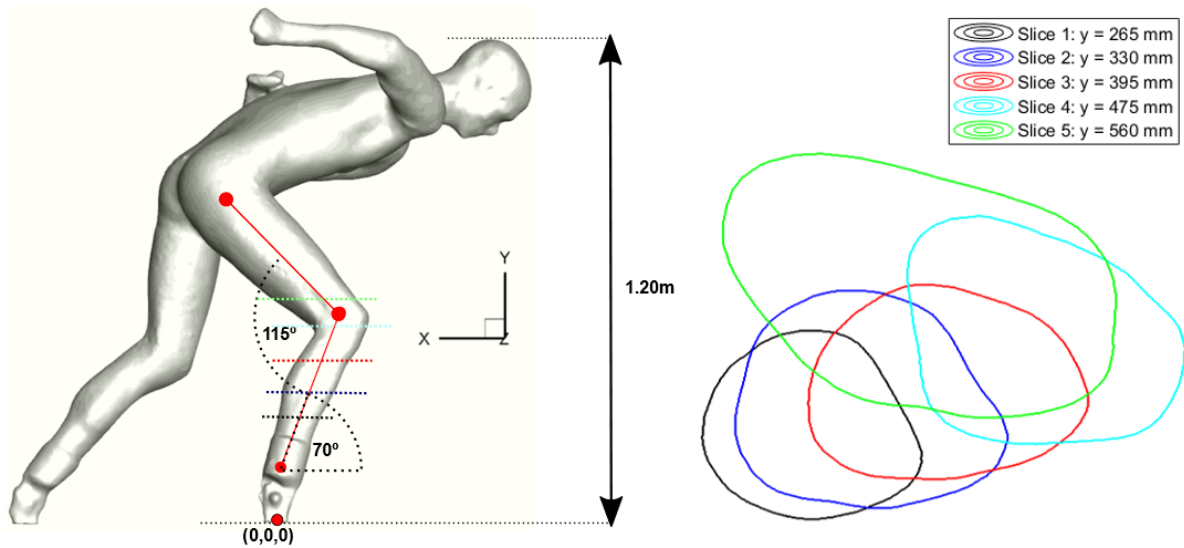


Figure 3.1: Side view of the 3D model of the skater mannequin, together with the coordinate system and its origin, ankle and knee angle and height of the mannequin. Next to this, a top view of the different cross-sections of the leg is shown. The heights of the different cross-sections are indicated by the colored dashed lines on the model.

In the results section, the wake profile is analysed at different heights across the leg. The top view of their cross-sections is also shown in figure 3.1. The cross-sections either have a more circular or a more elliptical shape. Their shapes obviously affect the flow around these cross-sections. This effect is discussed in more detail in the results section. The length, width and ratio of the individual cross-sections are shown in table 3.1.

Table 3.1: Length, width and ratio of the five different selected cross-sections that are shown in figure 3.1.

	Length [cm]	Width [cm]	length/width [-]
<b>Slice 1</b>	11.0	9.5	1.16
<b>Slice 2</b>	13.7	10.9	1.26
<b>Slice 3</b>	14.1	9.8	1.44
<b>Slice 4</b>	14.0	11.5	1.22
<b>Slice 5</b>	19.7	13.3	1.48

For both the PIV and IT set-up, the mannequin is connected with two bolts to a steel plate. This steel plate is enclosed by two wooden ground plates and is connected to a force balance measurement system that measures the forces and moments in X, Y and Z direction. Force balance measurements have been performed for the full velocity sweep for the bare mannequin and the dressed mannequin. To minimize the interference of the floor boundary layer with the flow around the mannequin, the complete set-up is elevated 30 cm above the tunnel outlet. The seeding system is placed right before the contraction area of the tunnel. Figure 3.2a and 3.2b respectively show a schematic drawing and a picture of the PIV set-up.

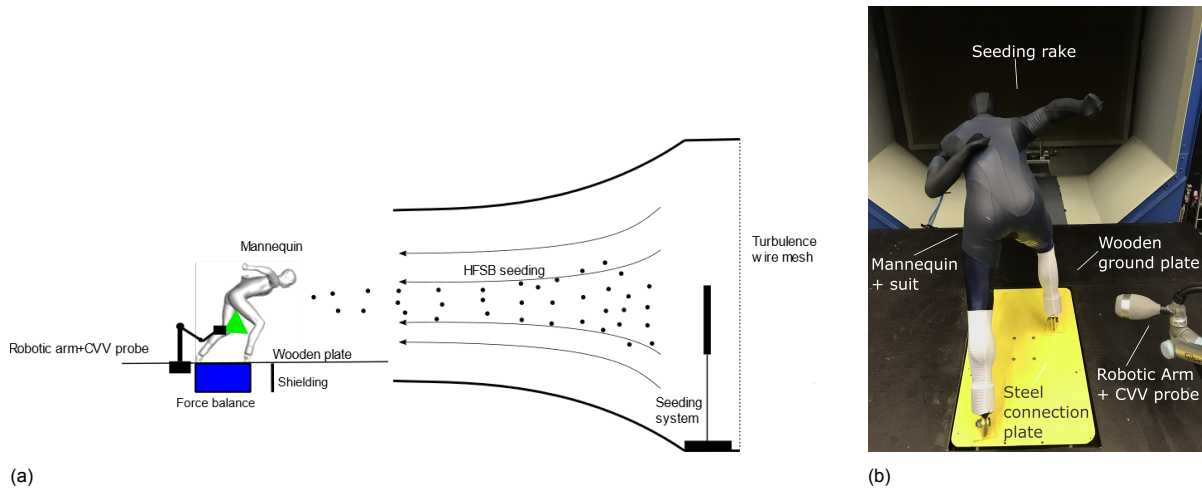


Figure 3.2: (a) Schematic drawing of the side view of the PIV set-up and (b) Picture of the PIV set-up including the naming of the relevant items.

Figure 3.3a and 3.3b respectively show a schematic and a picture of the IT set-up, among others, indicating the camera and heat source positions. The right leg is heated from both sides by two different halogen construction lamps.

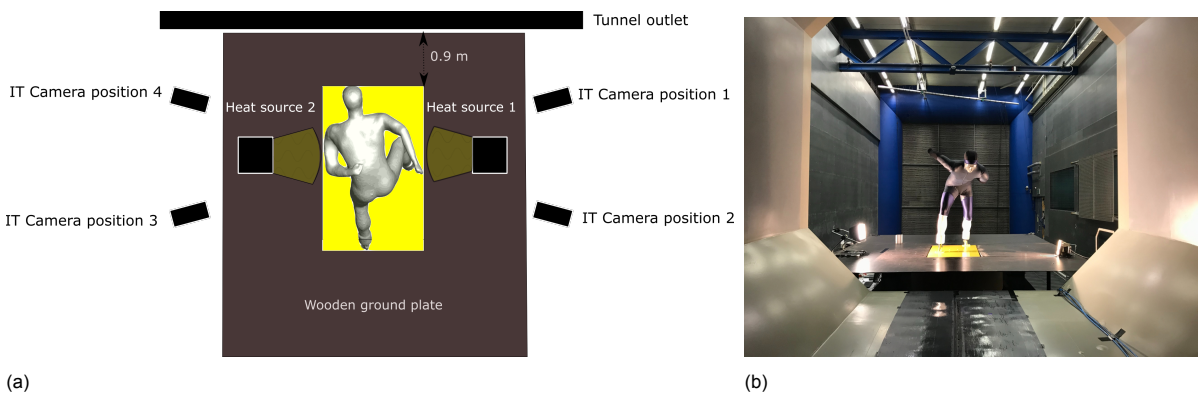


Figure 3.3: (a) Schematic of the top view of the IT set-up and (b) Picture of the IT set-up in which the leg of the mannequin is heated by the two heat sources.

### 3.2. Measurement equipment-Robotic PIV

Coaxial Volumetric Velocimetry robotic PIV is used to measure the flow field around the skater leg. The LaVision GmbH minishaker aero CVV probe consists of 4 CMOS cameras together with an optical fibre in the centre of the probe that delivers the light coming from the Quantronix Darwin Duo Nd:YLF laser head. The laser has a pulse energy of 25 mJ at 1 kHz and the laser beam is diverged by a lens, producing a conical illuminated volume. The technical specifications of the CVV probe are shown in table 3.2. The measurement domain can be extended by displacing the CVV probe. These displacements are realised by connecting the CVV probe to a six degree of freedom Universal Robots UR5 robotic

arm that consists of 6 joints. The robotic arm has a maximum reach of 85 cm radius around its base and a positional repeatability of  $\pm 0.1$  mm [2]. Aerodynamic interference effects from the robotic PIV system are reported to be less than 2% [12]. A more detailed explanation on (robotic) PIV is provided in appendix C.

HFSB are used as tracer particles, having a size of around 0.3 mm and a density similar to that of air. The particles are generated by a seeding rake with a height and width of 1.0 m and 0.5 m respectively. The seeding rake comprises 204 nozzles, generating  $\sim 40,000$  particles per second per nozzle. The seeding rake has little effect on the turbulence intensity. N. Mahalingesh (2019) reported an absolute increase by 0.61% and 0.01%, at respectively 5 and 15 m/s, measured in another low-speed wind tunnel at the Technical University of Delft [19].

Data reduction techniques are applied to the recordings and are discussed in more detail in appendix D. After applying the reduction techniques, the recordings of the different positions are merged and divided into bins of  $3.3 \times 3.3 \times 3.3 \text{ cm}^3$  with a 75% overlap and a minimum number of 20 particles inside each bin. After the binning, the results are evaluated in Tecplot and Matlab.

Table 3.2: Technical specifications of the LaVision MiniShaker Aero CVV probe.

<b>Optics</b>	Focal length	4 mm
	Numerical aperture (at $z_0=400$ mm)	11
<b>Imaging</b>	X tomographic aperture	$8^\circ$
	Y tomographic aperture	$4^\circ$
	Sensor size	$640 \times 475 \text{ px}^2$
	Pixel pitch	$4.8 \mu\text{m}$
	Magnification (at $z_0=400$ mm)	0.01
	Bit depth	10 bit
	Maximum acquisition frequency	821 Hz

### 3.3. Measurement equipment-Infrared Thermography

For the IT measurements, the leg is heated with the two available light sources, of 500 W and a 1000 W, on respectively the left and right side of the leg. At the same time, the leg is cooled down by the airflow. A similar approach, that yielded reliable results, has been applied by Kuklova et al. (2012). The radiated surface heat is captured from four different angles with Optris PI 640 Infrared cameras, with an O15 Tele lens mounted to it. The technical specifications of the camera and its lens are listed in table 3.3.

Table 3.3: Technical specifications of the Optris PI 640 Infrared camera and its lens retrieved from Optris [1].

Accuracy	$\pm 2 \text{ }^\circ\text{C}$ or $\pm 2\%$ , whichever is greater
Optical resolution	$640 \times 480$ pixels
Spectral range	$8 - 14 \mu\text{m}$
Frame rate	32 Hz
Thermal sensitivity (NETD)	75 mK
IFOV at ( $z_0 = 2\text{m}$ )	0.8 mm
Focal length	41.5 mm

### 3.4. PIV measurement uncertainty

The uncertainty of the time-average velocity, measured by the CVV probe, is dominated by statistical (random) errors. Therefore, the relative uncertainty is determined, using equation 3.1 [27].

$$\epsilon_u = \frac{k\sigma_u}{U_\infty\sqrt{N}} \quad (3.1)$$

With  $\epsilon_u$  the relative uncertainty,  $k$  the coverage factor,  $\sigma_u$  the standard deviation of the streamwise velocity,  $U_\infty$  the free-stream velocity and  $N$  the number of particles inside a bin. The difference in

uncertainty within the measurement domain is dominated by  $N$ . Closer than  $\sim 0.1$  m to the probe, the number of particles significantly decreases, this also holds for a distance of more than  $\sim 0.5$  m from the probe. The relative uncertainty in these domains at 95% confidence level ( $k=1.96$ ) approximately is 1.5%, with  $\sigma_u/U_\infty \sim 0.17$  and  $N \sim 500$ . Within the range of 0.1 m - 0.5 m distance to the probe the uncertainty approximately is 0.15%, with  $\sigma_u/U_\infty \sim 0.17$  and  $N \sim 50.000$ . The uncertainty of the critical velocity  $\epsilon_{v,crit}$  depends on the absolute difference between the consecutive free-stream velocities. For  $U_\infty = 5-10$  m/s and for  $U_\infty = 20-25$  m/s, this uncertainty is equal to  $\epsilon_{v,crit} = 2.5$  m/s. Between 10 m/s and 20 m/s,  $\epsilon_{v,crit}$  is equal to 1.25 m/s. The uncertainty of the wake width evaluation is determined similarly as determined by Terra et al. 2020 [32]. The wake width uncertainty is defined as  $\epsilon_{dw} = \sqrt{2}h$ , for which  $h$ , the spacing between adjacent velocity vectors, is equal to 8.2 mm. This results in an  $\epsilon_{dw}$  of  $\sim 11.5$  mm.

## 4. Results

### 4.1. Force balance measurements

Force balance measurements have been performed to evaluate if the suit, when worn by the mannequin, causes a reduced  $C_D A$  with respect to the bare mannequin. Figure 4.1 shows these results, in which  $C_D A$  is plotted against the free-stream velocity. The graph demonstrates the significant reduction of  $C_D A$ , caused by the suit, for  $U_\infty > 5$  m/s. The error bars indicate the accuracy of the force balance. Furthermore, the typical racing speeds for men skaters, at respectively the 10 k, 1500 m and 500 m are indicated by the green vertical domains.

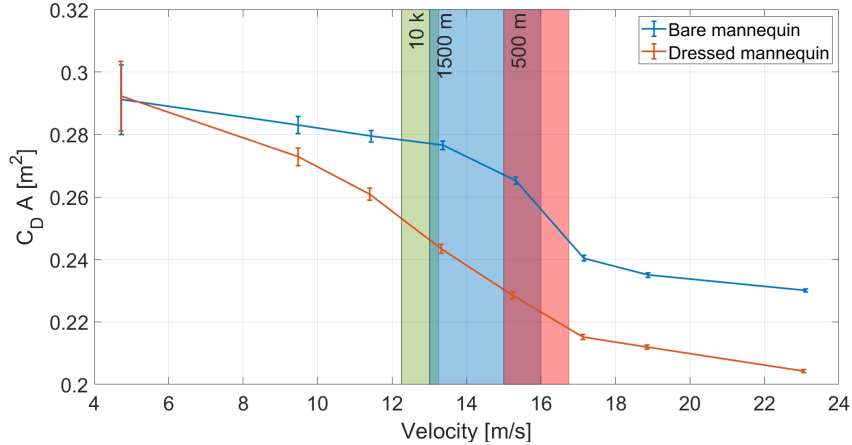


Figure 4.1: Results of the force balance measurement, in which the  $C_D A$  of the bare mannequin is compared with the  $C_D A$  of the dressed mannequin, for increasing velocity. The error bars indicate the accuracy of the measurement device and the vertical domains indicate the velocity range for men skaters during a race at, from left to right, the 10 k (green), 1500 m (blue) and 500 m (red).

### 4.2. Global flow characteristics

#### 4.2.1. Bare mannequin

The wake flow topology of the bare mannequin is evaluated at typical racing speed, namely  $U_\infty = 15$  m/s. Results are obtained using the robotic PIV technique and are visualized in the top row of figure 4.2. Sub-figure 4.2a shows the non-dimensional time-average streamwise velocity contours in the  $y$ -plane at five different heights. It depicts the free-stream regions on both sides of the leg and the reduced streamwise velocity behind the leg. Behind the lower leg, areas of reverse flow are present. It should be noted that these areas seem relatively small. This can at least partly be ascribed to the masking function that is applied during image processing and is discussed in more detail in appendix D.1. The maximal downstream extension of the recirculation region occurs at  $y = 330$  mm and is located at the widest section of the lower leg. Behind the upper leg, a recirculation region is not present, indicating that no flow separation seems to occur. The reduced velocity deficit locally decreases the drag and is caused by the inclination of the leg. Similar features of a reduced velocity deficit for inclined cylinders were also found by Zhou et al. (2009) [35]. Furthermore, an inwards deflection of the upper leg wake profile is observed, most probably because of wake interference with the upper left leg of the skater.

The top row of sub-figure 4.2b visualizes the iso-surface of the non-dimensional time-average streamwise velocity of  $U_x/U_\infty = 0.2$  for the bare leg. The width of the iso-surface behind the lower leg is roughly proportional to the leg width and both are widest around  $y = 330$  mm. Sub-figure 4.2c depicts the streamlines, coloured by the non-dimensional time-average streamwise velocity, among others showing the recirculation region behind the calf. Also, the streamlines behind the upper leg are pointing slightly upwards and behind the lower leg are slightly pointing downwards and is caused by the inclination of the leg. The latter effect is also reported in literature for inclined cylinders [20].

Sub-figure 4.2d shows the time-average streamwise vorticity combined with in-plane vectors and contour lines that are set by the Q-criterion at  $x = 70$  mm. Anti-clockwise streamwise vorticity is observed behind the right side of the calf. Also, a pair of counter-rotating streamwise vortices is observed just above the knee. This pair of vortices cause the development of an upward flow along the upper leg, annihilating the separation region behind the upper leg. The upward flow along the upper leg and the vanishing of the separation region are both supported by, respectively the streamlines of sub-figure 4.2c that slightly point upwards behind the upper leg and the recirculation region that is not observed behind the upper leg in sub-figure 4.2a.

Lastly, part of the figure 4.2b is marked with a dashed ellipse, indicating the noise that is present behind the upper leg. This noise most likely stems from the edge effects, since it is located on the boundaries of the measurement domain<sup>1</sup>. Furthermore, a lateral deflection of the iso-surface at the lower leg is observed in figure 4.2b, indicated by the black arrow. The lateral deflection might be caused by the aforementioned anti-clockwise rotating vortices behind the calf, but can also be a result of the non-symmetric leg shape.

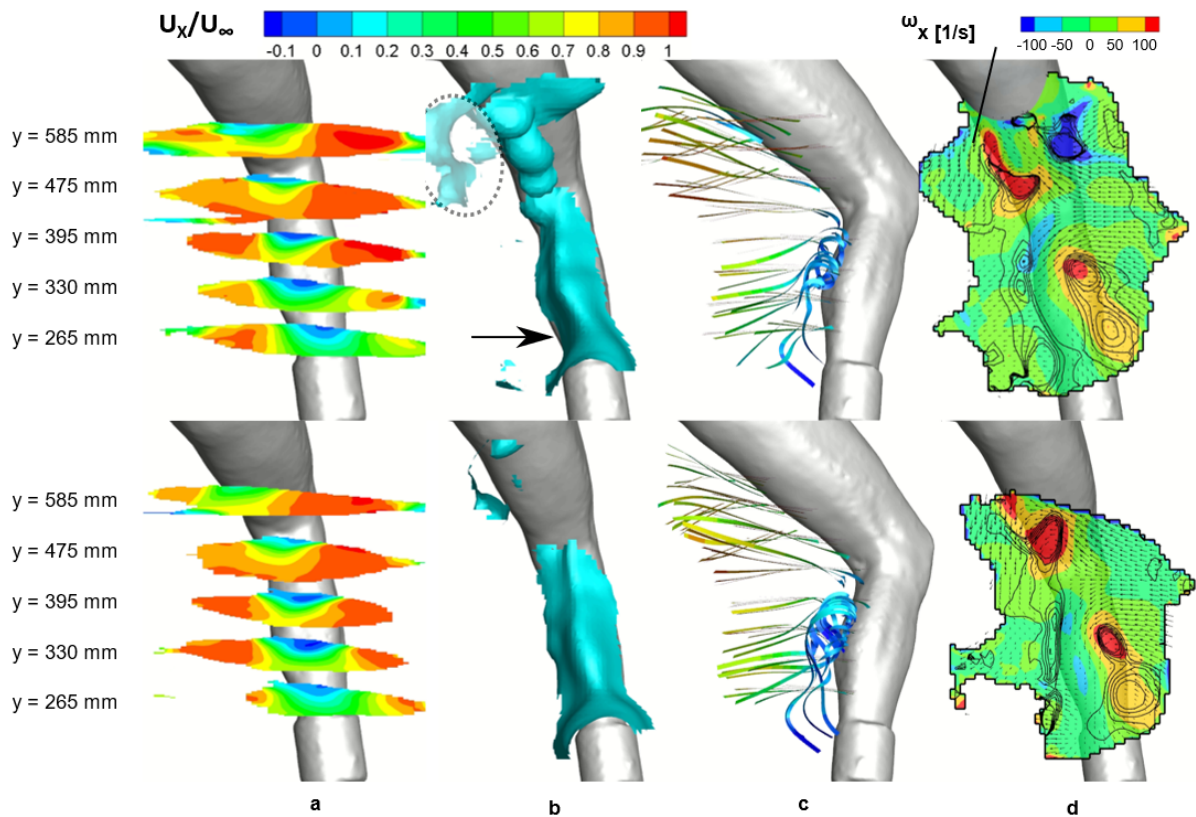


Figure 4.2: Visualization of the non-dimensional time-average wake flow topology of the bare leg (top row) and the dressed leg (bottom row), at  $U_\infty = 15$  m/s. With **a**): streamwise velocity contours in the y-plane at five different heights, **b**): iso-surface of the streamwise velocity of  $U_x/U_\infty = 0.2$ , **c**): streamlines coloured by the streamwise velocity and **d**): streamwise vorticity combined with in-plane vectors and contour lines set by the Q-criterion ( $x = 70$  mm).

#### 4.2.2. Dressed mannequin

Similar to the bare mannequin, the wake flow topology at  $U_\infty = 15$  m/s is now visualized for the dressed mannequin and is shown in the bottom row of figure 4.2. The wake flow topology shows high similarities with the one of the bare mannequin, such as the wake deflection at the upper leg, and the anti-clockwise streamwise vorticity behind the right side of the calf.

<sup>1</sup>Edge effects arise on the outer boundaries of the measurement domain and are caused by particles that are too far away from the probe and therefore do not reflect enough light to yield meaningful physical results.

However, differences are also observed. Most remarkable is the reduction of the velocity deficit behind the upper leg and is most likely due to the suit. Hence, no  $U_x/U_\infty = 0.2$  iso-surface is present behind the upper leg which locally decreases the drag that is experienced by the upper leg.

Next to this, for the dressed mannequin in sub-figure 4.2d, a pair of counter-rotating streamwise vortices behind the upper leg is not observed. At  $U_\infty = 15$  m/s, the measurement domain of the bare leg at  $x = 70$  mm extends further in the  $y$ -direction compared to the dressed leg. However, no counter-rotating vortex pair is observed for any of the free-stream velocities behind the upper leg of the dressed mannequin. This is in contrast with flow behind the bare mannequin, for which a counter-rotating vortex pair is present at all free-stream velocities. Still, the anti-clockwise streamwise vorticity behind the inner side of the thigh causes an upwash on the upper leg, annihilating the separation region behind the upper leg.

### 4.3. Reynolds number effects: Comparison between the bare and the dressed leg

#### 4.3.1. Spanwise non-dimensional velocity profiles at different free-stream velocities

The non-dimensional velocity profiles at different free-stream velocities in the wake of the bare and the dressed leg are analysed at five different heights along the leg. Differences in wake profile were most pronounced for  $y = 265$  mm, 395 mm and 475 mm and are shown in figure 4.3. The non-dimensional streamwise velocity is measured at a distance behind the leg of 1.1 times the leg width. Its position is indicated by the red dots behind the leg of figure 4.3. In general, differences in wake profile are most pronounced for the dressed leg. The latter is most probably caused by the distributed roughness on the suit that forces a transition to the critical regime, showing larger variations in wake width.

When looking at the spanwise velocity profiles of the bare leg at  $y = 265$  mm, the wake profiles of  $U_\infty = 5$  m/s and 10 m/s are oriented more inwards. Also, the free-stream velocity is not reached on both sides of the leg, because of velocity data that is not captured within the  $z$ -domain. Reverse flow is present for all free-stream velocities at  $y = 260$  mm, whereas this only holds for  $U_\infty = 5$  m/s, 10 m/s and 25 m/s for the dressed leg. This decreased velocity deficit is most likely caused by the distributed roughness on the suit of the dressed leg and has the effect of locally reducing the drag.

For the bare mannequin at  $y = 395$  mm, the wakes of  $U_\infty = 5$  m/s, 10 m/s and 25 m/s clearly are wider than for the other free-stream velocities. The larger velocity deficit for the latter free-stream velocities is inherent to higher drag. It could also indicate that for  $U_\infty = 5$  m/s and 10 m/s the flow is still in the sub-critical regime, whereas for  $U_\infty = 25$  m/s, the flow is in the super-critical flow regime. For the dressed leg, the variations in wake width and minimum non-dimensional velocity are even more pronounced. At  $U_\infty = 25$  m/s, the minimum non-dimensional wake velocity is significantly lower. For the latter free-stream velocity also the highest velocity deficit is observed and therefore most likely experiences the highest local drag. Based on the small velocity deficit, the drag seems least for  $U_\infty = 12.5$  m/s.

At  $y = 475$  mm, the wake profiles of the bare leg are hardly affected by the free-stream velocity. However, the results are again more pronounced for the dressed leg. For both configurations, the wake profiles are more oriented to the left and is due to the inwards orientation of the cross-section at this particular height. For the dressed leg at  $y = 475$  mm, the velocity deficit is larger for  $U_\infty = 5$  m/s, 20 m/s and 25 m/s, which could again indicate that the flow is in the sub-critical regime at  $U_\infty = 5$  m/s and in the super-critical regime for  $U_\infty = 20$  m/s and 25 m/s.

#### 4.3.2. Local wake width

The non-dimensional wake widths of the bare and the dressed leg are determined across the height of the leg between  $y = 215 - 575$  mm. The non-dimensional wake widths are determined by dividing the local wake width by the local width of the leg. Most significant changes between the bare leg and the dressed leg are observed at 17.5 m/s. The comparison between these configurations is shown in figure 4.4. The three different regions on the leg are determined based on the leg geometry. In general, a somewhat linear decrease of the non-dimensional wake width is observed in the lower leg region. This can partly be ascribed to the increasing length-width ratio of the lower leg, meaning that the lower leg becomes more 'streamlined' when increasing the height. Secondly, this larger wake width in the lower part of the lower leg is due to the anti-clockwise streamwise vorticity that locally increases the wake

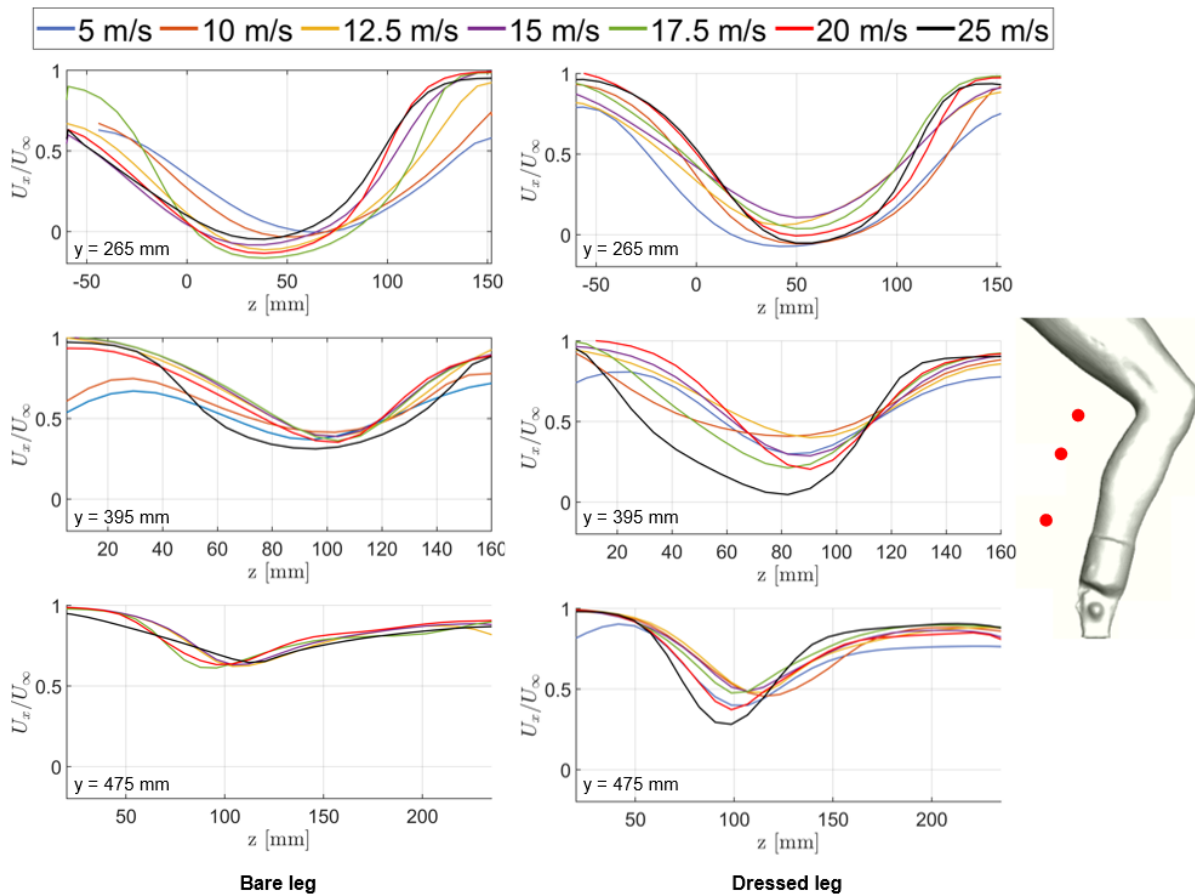


Figure 4.3: Non-dimensional time-average spanwise velocity profiles in the wake of the bare leg (left) and in the wake of the dressed leg (middle) measured at three different heights along the leg. The height and position behind the leg are indicated by the red dots behind the leg (right).

width. The smallest wake widths are observed in the knee region. Despite the pronounced differences of the wake profile in the knee region of the dressed leg, discussed in section 4.3.1, wake width variations are small in this area. The non-dimensional wake width could only be determined for a small part of the upper leg. Also, the non-dimensional wake widths for the upper leg are relatively small. This is ascribed to upwash on the upper leg caused by the pair of counter-rotating vortices behind the leg. Furthermore, because of the upper leg inclination, the cross-sections of the upper leg are relatively streamlined.

When comparing the non-dimensional wake width of the bare and the dressed leg at 17.5 m/s, differences are most pronounced in the lower leg region, with a maximum wake width reduction of around 45%, at  $y = 315$  mm. The latter is most probably due to the high similarities between the lower leg and a cylinder in cross-flow, for which distributed roughness is known to effectively reduce the drag by forcing an earlier transition from the sub-critical to the critical flow regime. In the knee and upper leg region, differences in wake width are small. This could either indicate that the wake width depends less on the free-stream velocity and thus is mainly dominated by streamwise vortices that emanate just above the knee. Or that the flow for both configurations does not feature drag crisis behaviour, which is less likely to be true for the knee region because of the substantial differences in wake profile that are observed for the dressed mannequin in figure 4.3.

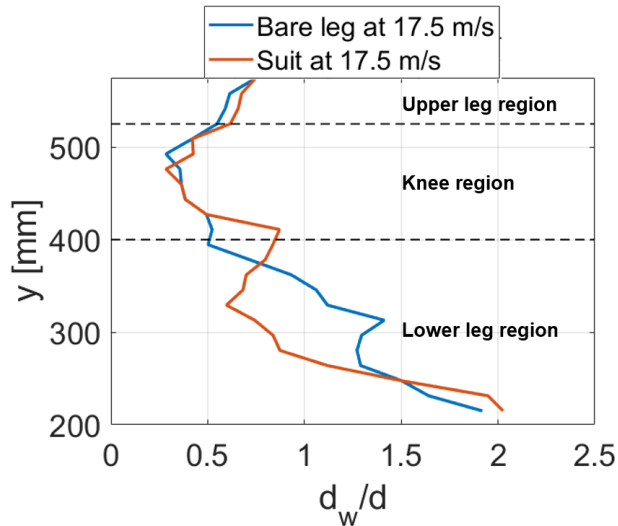


Figure 4.4: Comparison of the non-dimensional wake width across the leg between the bare and the dressed leg at 17.5 m/s.

4.3.3. Critical velocity

The critical velocity at which the drag crisis occurs is determined based on the free-stream velocity for which the wake width is minimal. It should be stressed though, that the existence of the critical velocity is not guaranteed, since it is unknown if the flow across the leg features drag crisis behaviour. Figure 4.5a and 4.5b show the non-dimensional wake widths for increasing free-stream velocity at five different heights, for respectively the bare and the dressed leg.

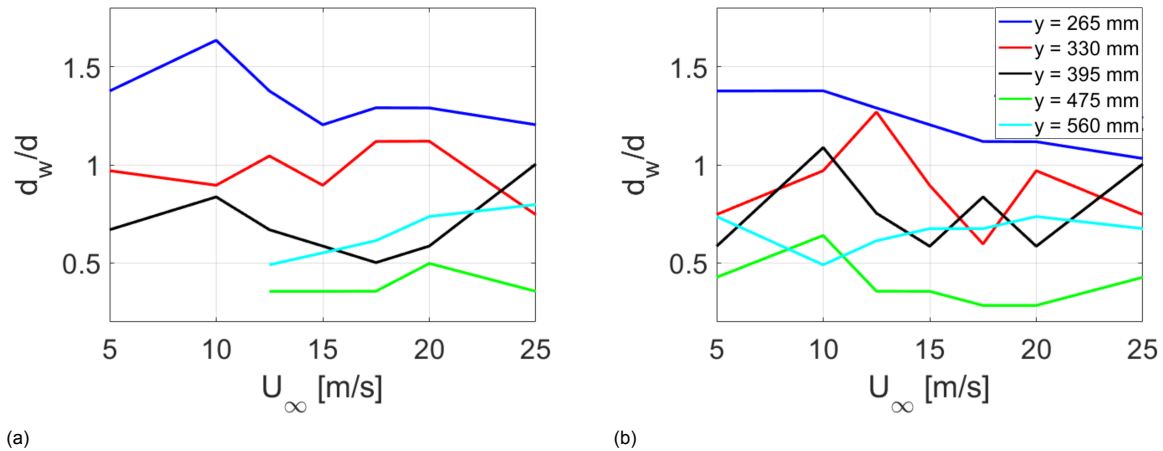


Figure 4.5: Non-dimensional wake width of the bare mannequin (a) and the dressed mannequin (b) at five different heights for increasing velocity.

At  $y = 265$  mm, the critical velocity for the bare leg, when existing, most likely is  $\geq 25$  m/s. For  $U_\infty \geq 15$  m/s the wake width is nearly constant, but the wake width is expected to decrease for  $U_\infty \geq 25$  m/s, since for the suit, the blue line is also still decreasing at this point. The smaller wake width for the suit at  $U_\infty = 25$  m/s compared to  $U_\infty = 20$  and 17.5 m/s could be due to the measurement uncertainty of the wake width evaluation, being  $\sim 11.5$  mm, as determined in section 3.4. Therefore, the critical velocity at  $y = 265$  mm for the suit is expected to be around  $U_\infty = 20$  m/s. At  $y = 300$  mm, the critical velocity for the bare leg, likely is  $\geq 25$  m/s, because of the strong wake width reduction from 20 m/s to 25 m/s. For the dressed leg, the wake width already starts decreasing at  $U_\infty = 10$  m/s, indicating a local drag reduction. The minimum wake width for the dressed leg is observed for  $U_\infty = 17.5$  m/s, most likely being the critical velocity, thus showing drag crisis behaviour. The latter is in line with the findings observed by D’auteuil et al. (2012). They also observed drag crisis behaviour at the calf of the

mannequin's standing leg, while in side-push position for turbulent flow conditions [10].

At  $y = 395$  mm, a clear minimum wake width is observed for the bare leg at  $U_\infty = 17.5$  m/s. However, for the dressed leg, a clear minimum wake width cannot be found, but when existing, the critical velocity is expected somewhere near 15 m/s, because of the significant drop between 10 m/s and 15 m/s. Moreover, the suit is expected to force a shift to a critical velocity that is lower than for the bare leg. At  $y = 475$  mm, which is at knee height, the minimum wake width for the bare leg cannot be determined due to missing data at 5 m/s and 10 m/s. For the dressed leg, the critical velocity is close to 17.5 m/s. At  $y = 560$  mm, an almost linear increase of the non-dimensional wake width is observed for the bare leg. Hinting at a critical velocity of  $\leq 12.5$  m/s. For the dressed leg, a minimum wake width is observed at 10 m/s, suggesting it to be the critical velocity. Overall, due to the significant changes in wake width for increasing velocity, drag crisis seems to occur along the five different evaluated heights, thus is encountered for the lower leg, knee and upper leg region.

#### 4.3.4. Optimal suit performance

It is assumed that the most optimal performance in terms of drag reduction is realised when the wake width is minimal. Therefore, the minimum non-dimensional wake width that was measured at each height, is compared with the non-dimensional wake width of the dressed leg at 15 m/s. In this way, it is evaluated how close the dressed leg approaches the minimal measured wake width at typical racing conditions. Results are shown in figure 4.6. Showing that, with an average percentage of around 20% possible wake width reduction, the wake widths for all three regions still can be reduced. When encountering this minimal measured wake width along the leg, the lap time of a skater will be reduced by  $\sim 0.85$  s, while producing an average power of  $\sim 510$  W. The potential time reduction is determined with respect to the dressed leg at 15 m/s. The corresponding calculations are shown in appendix E.

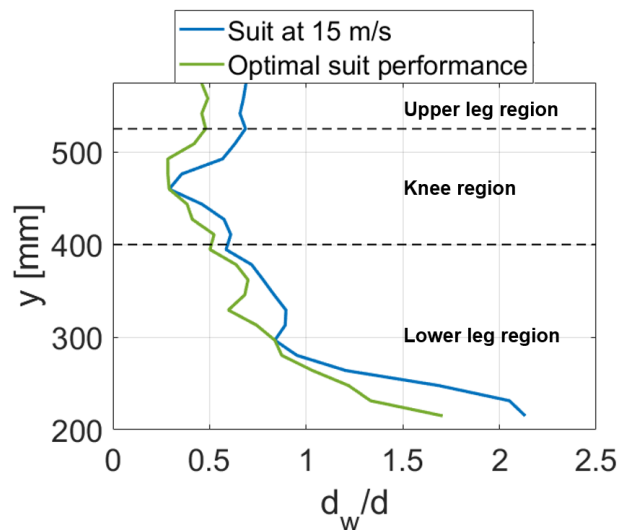


Figure 4.6: Comparison of the non-dimensional wake width across the leg between the dressed leg at 15 m/s and the minimum non-dimensional wake width that was measured.

#### 4.4. Infrared Thermography

The flow across the leg of the mannequin is visualized, using Infrared thermography. Four of these results are shown in figure 4.7. All configurations are captured from the right side of the leg as shown on the right of figure 4.7. The colour bar indicates the absolute temperature difference between the zero measurement (wind-off configuration) and the actual measurement (wind-on configuration)<sup>2</sup> and is defined as  $\Delta T$ . The reddish areas on the leg indicate the regions of high cooling, caused by the flow. The bluish areas, on the other hand, indicate the regions of reduced cooling. Lastly, flow separation is recognized by the dark blue regions on the surface.

The areas of reduced cooling are mainly observed for the bare and the dressed leg at 5 m/s, most likely indicating the presence of a laminar boundary layer. The flow separates at the position of the red drawn lines and is approximately equal for both configurations. When increasing the free-stream velocity to 15 m/s, as expected more surface cooling is observed on the bare and the dressed leg, pointing at the presence of a turbulent boundary layer. Again, the flow separation is indicated by the drawn red lines on the leg. However, more upstream just below the knee, a second separation line seems present, indicated by the black arrow. Beyond this dark blue line, the cooling rate increases again and possibly indicates the presence of a laminar separation bubble that reattaches as a turbulent boundary layer. The latter effect postpones the flow separation, resulting in locally reduced drag.

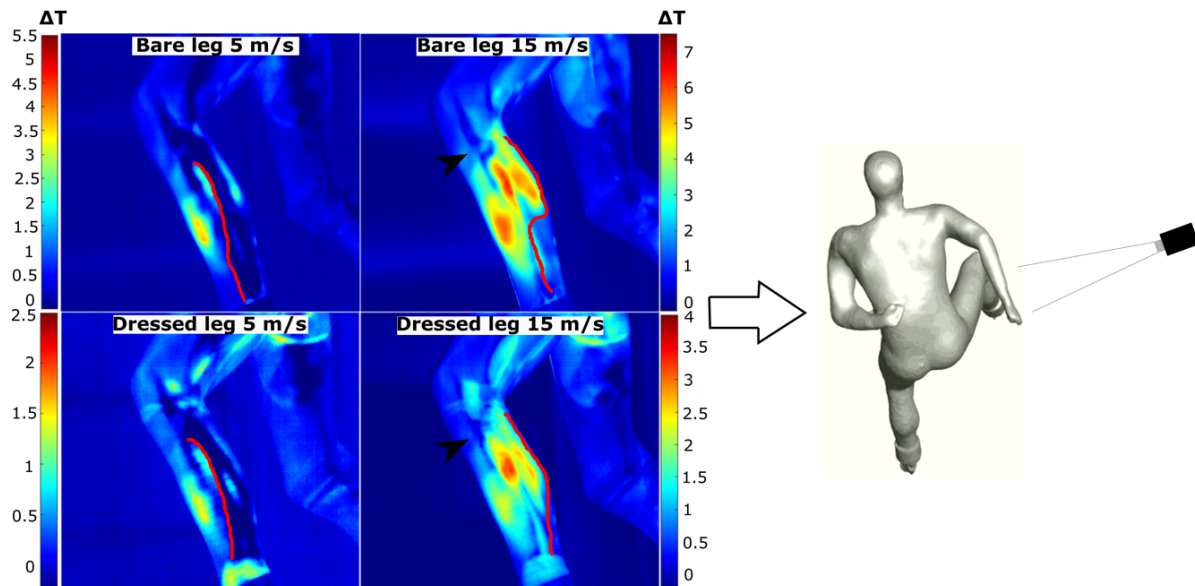


Figure 4.7: Visualization of the flow across the bare leg (top row) and the dressed leg (bottom row) at 5 m/s and 15 m/s by means of Infrared Thermography. The colour bar indicates the absolute temperature difference  $\Delta T$  between the wind-on and wind-off configuration. Locations of flow separation are indicated by the black arrows and/or drawn red lines on the surface. The right figure shows the camera position.

As discussed in subsection 4.3.2, a substantial difference in wake width for the lower leg was observed between the bare and the dressed leg at  $U_\infty = 17.5$  m/s. A narrowing wake width goes along with a relocation of the point of flow separation further downstream. To evaluate this, the locations of the separation lines for both configurations are compared with each other on the right side of figure 4.8. The results are again captured from the same position as figure 4.7. Just below the knee, approximately in the centre of the leg, the separation occurs further downstream for the bare leg. As expected, the distributed roughness forces an earlier transition from a laminar to a turbulent boundary layer. When looking further downstream, the separation positions seem similar for the upper part of the leg. Although, it is more difficult to compare the location since these separation lines are located at the border of what is visible from this camera angle<sup>3</sup>. On the lower part of the lower leg, the point of

<sup>2</sup>The colour scales of the bare and the dressed leg are not identical because of the difference in emissivity between the configurations.

<sup>3</sup>Due to displacement of the camera that was positioned behind the leg, no fair comparison regarding the location of separation could be made. Therefore, results captured further downstream are omitted.

separation on the dressed leg is located significantly further downstream. The latter is caused by the distributed roughness on the suit that triggers a boundary layer transition and postpones the separation. This observation is supported by the results of figure 4.4.

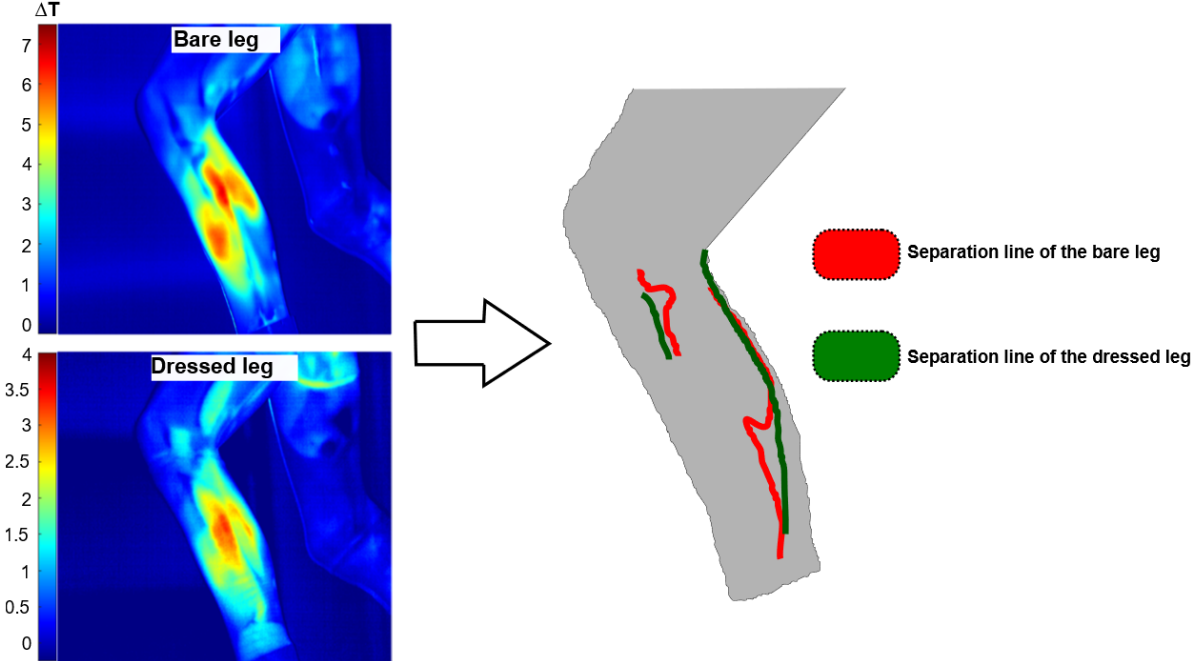


Figure 4.8: Visualization of the flow across the bare and dressed leg, at  $U_\infty = 17.5$  m/s, by means of Infrared Thermography (left) and contours of the separation line for both configurations (right). The colour bar indicates the absolute temperature difference  $\Delta T$  between the wind-on and wind-off configuration. Results are captured from the same position as figure 4.7.

## 5. Discussion

In literature, much of today's knowledge related to skating aerodynamics has been obtained by studying the flow across bluff bodies. However, the question to what extent these flow features are similar to the flow features around a skater so far remained unanswered. With this study, this knowledge gap has been partly filled by studying the Reynolds number effects along the standing leg of a skater mannequin utilizing robotic PIV and IT. The PIV measurements revealed significant variations in wake width for the lower leg, knee and upper leg region and a considerable change in wake profiles for the lower leg and the knee region, both revealing drag crisis behaviour. In addition to the PIV measurements, the IT measurements also revealed typical drag crisis behaviour in terms of relocation of the flow separation further downstream for the dressed leg, indicating a local drag reduction caused by the suit.

Important features such as the upwash of air on the upper leg, caused by strong positive and negative streamwise vorticity were revealed. The latter phenomenon is also reported in literature for inclined cylinders [20] and locally reduces the velocity deficit behind the upper leg. The reduced velocity deficit behind the upper leg was even more pronounced for the dressed mannequin. Furthermore, strong anti-clockwise streamwise vorticity was observed behind the right side of the calf, increasing the wake width of the lower leg below the calf. The presence of these vortices certainly should be taken into account when evaluating the drag reduction performance of fabrics on isolated cylinders.

As mentioned in the introduction, D'outeuil et al. (2010) observed that flow interaction between the different body parts affected the choice of the optimal fabric. In the present study, the flow topology was only evaluated for the right leg and only one skating suit. Therefore, no conclusion can be drawn on whether the present study supports these findings. However, phenomena such as the positive and negative streamwise vorticity that emanate from the leg and the side-wise wake deflection of the upper leg, most likely because of wake interference of the left leg, are indications that this particular statement of D'outeuil et al. (2010) may be correct. Accordingly, choosing fabrics purely based on the results of isolated cylinder measurements could easily lead to a less optimal fabric choice, because of the highly complex flow dynamics.

The present study also has some limitations. First of all, the local wake width could only be determined up to a height of  $y = 575$  mm. Above this height, data coverage was not sufficient at the inner side of the leg. The latter is most probably caused by a too large distance between the probe and the wake of the upper leg. Resultingly, the critical velocity could not be determined along the full length of the leg. Furthermore, in some cases either the velocity range was too small or  $\epsilon_{dw}$  was too large to accurately determine the critical velocity. Extending the velocity range and reducing  $\epsilon_{dw}$ , but certainly also  $\epsilon_{v,crit}$  would improve the accuracy of the critical velocity determination.

Additionally, it should be stressed that the findings of this study may differ from feature research that is related to skating aerodynamics. The latter could be the case when a different skating mannequin is used, which likely will have different dimensions. A different leg width or inclination of the leg for example definitely will affect the critical Reynolds number. Despite the possible variation in geometry and position, the present study still provides a useful indication of the main flow features around a skater. Another limitation of the present study is the fact that the flow is only captured for one particular static skating position. The Reynolds number effects most likely will be different when evaluating different skating positions or when evaluating the flow around a moving skater. Skaters may also experience a different level of free-stream turbulence during a race. Free-stream turbulence has a significant effect on the drag crisis behaviour [10] and therefore definitely should be further investigated.

Lastly, measurements results could have been improved by using black fabrics for the lower leg. Due to the higher emissivity of the black fabric, a higher contrast ratio for the IT results could have been achieved. In addition, applying a black fabric on the lower leg minimizes the level of reflection which makes the application of the masking unnecessary. By not applying the masking, the small gap of missing data right behind the leg will be filled.

For future research, it is advised to investigate the complete wake flow topology of the skater to understand the Reynolds number effects along the full body of the skater. Also, different skating positions may be evaluated. Eventually, similar research may be performed on a moving skater.

## 6. Conclusion

The goal of this study was to investigate the Reynolds number effects along the leg of a skater and to study how these were affected by the surface properties of a skating suit. Therefore, the flow across the stance leg of a skater mannequin was evaluated for flow speeds ranging from 5 to 25 m/s, utilizing robotic PIV and IT. A comparison was made between the bare mannequin and the mannequin dressed up in a high-end skating suit. First, the drag reduction performance of the skating suit was analysed by performing force balance measurements. Then, the wake flow topology of both the bare and dressed leg were visualized and quantified via robotic PIV. Lastly, information on the boundary layer state and the location of separation on the leg was provided using IT. This has led to the following conclusions:

- Robotic PIV has revealed typical drag crisis behaviour along the lower leg, knee and upper leg of the skater by showing significant changes in the non-dimensional wake width with varying free-stream velocity.
- Differences in the non-dimensional wake width between the bare and the dressed leg were most pronounced in the lower leg region, especially for  $U_\infty = 17.5$  m/s.
- The robotic PIV results are supported by the IT results, revealing typical drag crisis behaviour through relocation of the separation line on the lower leg of the skater mannequin with varying free-stream velocity.
- A substantial reduction of the overall  $C_D A$  with respect to the bare mannequin of roughly 15% at  $U_\infty = 15$  m/s has been determined. This drag reduction at least partly stems from the stance leg of the mannequin and has been demonstrated by a relocation of the dressed lower leg separation line further downstream and a reduced velocity deficit behind the upper leg.
- The flow across the skater leg partly differs from cylinder flow since the drag crisis is not only governed by the leg geometry but also by strong streamwise vortices. This should be considered when designing a tailored skin suit, aiming at having minimum aerodynamic drag during a race.
- Based on the results of the present study, the potential lap time reduction that still can be achieved with respect to the dressed leg at 15 m/s, equals  $\sim 0.85$  s.

## A. Infrared Thermography

The Infrared Thermography (IT) measurement technique has not been employed for sports aerodynamics so far. However, IT has a significant benefit over other visualization techniques. This section shortly discusses the physics behind the technique, the type of IT measurement technique that is selected for the experiment and an example of the application of IT in a different field of research, showing the benefit over the oil flow visualization technique.

### A.1. Physics behind IT

Heat transfer is caused by temperature differences and is defined as the transfer of energy from one region to another. The transmission of heat can occur in three different ways. Namely by conduction, convection and radiation. Conduction is defined as the transfer of heat inside a medium. Convection is the transfer of heat caused by the movement of a fluid. Lastly, radiation is characterized by the emission of electromagnetic waves, without using any medium. The convection of heat is very similar to shear friction caused by the formation of a boundary layer. Equation (A.1) and (A.2) are showing the mathematical description of the shear friction and the surface heat transfer respectively.

$$\tau = \mu \frac{\partial u}{\partial y} \Big|_{y=0} \quad (\text{A.1})$$

$$q = -k \frac{\partial T}{\partial y} \Big|_{y=0} \quad (\text{A.2})$$

A laminar boundary layer has a smaller velocity gradient at the wall compared to a turbulent boundary layer, causing a lower shear stress for the laminar case. The same holds for the amount of heat transfer. Since for a laminar boundary layer, the temperature gradient will be lower than that of the turbulent boundary layer. This results in a heat transfer that is lower for a laminar than for a turbulent boundary layer. Also, at the location where a boundary layer separates, the shear stress and consequently the heat transfer will go to zero. Infrared thermography is a measurement technique that uses these physical principles, to distinguish the different flow regions on the surface of an object, with the help of one or multiple infrared cameras. The reason behind capturing the heat radiation in the infrared wavelength range is because at an ambient temperature most of the radiation is emitted in the infrared range.

### A.2. The steady active IT technique

For the Infrared thermography measurements, the active steady technique is used [27]. For the active steady technique, the model surface is first heated by one or multiple radiation sources, then the wind tunnel is activated which cools down the surface. After reaching a thermal equilibrium, the steady temperature is measured. This active method creates a high contrast, resulting in a very clear distinction between for example the laminar and turbulent boundary layer. With the Optris PI 640 Infrared camera, one can distinguish differences in the boundary layer state at levels of around 1 cm and greater. The width of a skater leg is in the order of  $1 \cdot 10^1$  cm, so the technique can be used to distinguish the different boundary layer states on a skater leg. The surface heat is captured with an accuracy of  $\pm 2$  °C or  $\pm 2\%$  (whichever is greater).

### A.3. Practical example

Kuklova et al. compared the oil flow visualization technique with visualization by the active infrared thermography technique on the suction side of an airfoil, shown in figure A.1 [15]. It is clear that the Infrared thermography technique, provides much more information about the development of the boundary layer and whether the boundary layer is laminar or turbulent. The surface is heated and has a low temperature at the leading edge. The laminar boundary layer starts to grow, resulting in less cooling and the heating of the surface. The red area in the centre of the airfoil is the point of separation where no cooling by convection occurs. After this, the boundary layer reattaches in a turbulent state, cooling the surface down again.

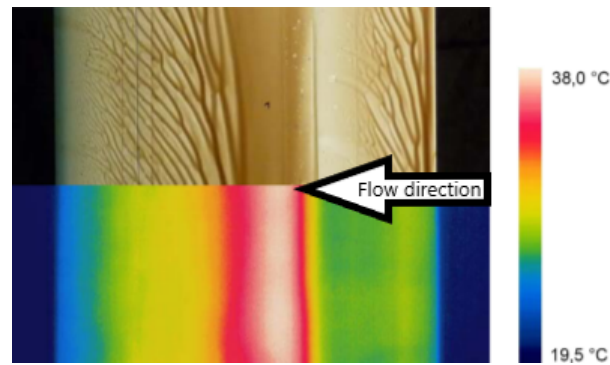


Figure A.1: Comparison between the oil flow visualization technique (top) and the visualization by the active infrared thermography technique (bottom) on an airfoil. The flow direction is indicated by the arrow. For both techniques the point of separation is equal and clearly visible and is located at the starting point of the vertical red line (bottom). In contrast to the oil flow technique, the IT technique (bottom) provides information on the state of the boundary layer over the complete surface of the airfoil [15].

## B. Suit figures

For the experiments, a state-of-the-art skating suit supplied by SportConfex, is used. The suit, worn by the mannequin, is shown in figure B.1.



Figure B.1: Figure of the skating suit used for the PIV and IT measurements.

Close-ups of the fabrics that are applied on the leg can be seen in figure B.2 and B.3 on the next page. The lower leg fabric and the fabric at the lower part of the thigh and the knee consist of a distributed roughness pattern. The distributed roughness pattern on the lower leg has a higher roughness compared to the fabric on the knee and part of the upper leg. The fabric at the upper part of the leg is a smooth material and is made out of polyurethane, which feels like a rubbery material.

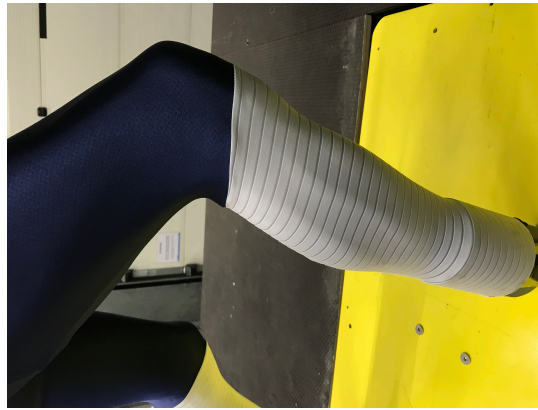


Figure B.2: Close-up of the skating suit used for the PIV and IT measurements, showing the two different fabrics with distributed roughness on the lower leg and thigh.



Figure B.3: Close-up of the skating suit used for the PIV and IT measurements, showing the smooth fabric and the fabric with distributed roughness on the upper leg.

## C. Particle Image Velocimetry

Particle Image Velocimetry (PIV), is a flow measurement method, that has developed over the past few decades. With this technique, small particles are introduced into the flow and illuminated by a LED or a laser. The flow field velocity is determined based on the particle displacement and the time between two consecutive images. A schematic of a typical PIV set-up is depicted in figure C.1.

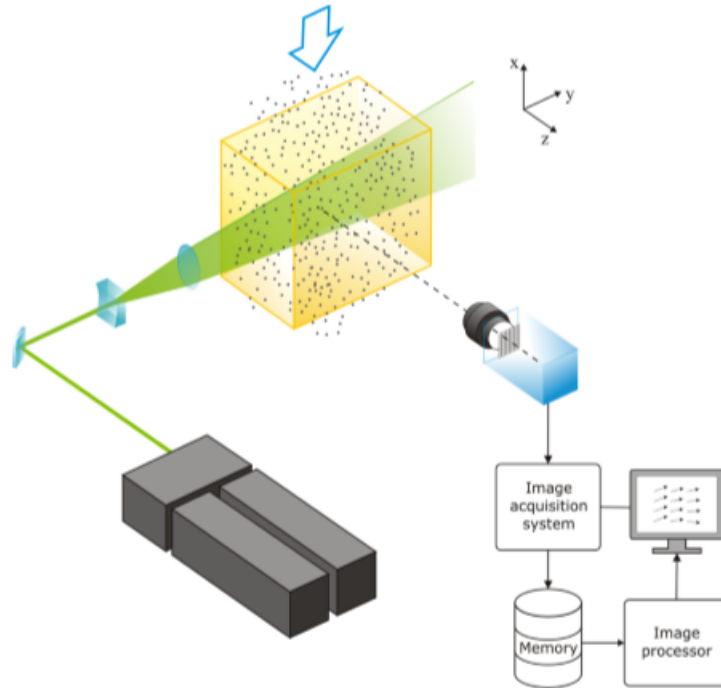


Figure C.1: Schematic of a typical PIV set up in which a 2D plane is illuminated by a light source [27].

An attractive benefit over other measurement techniques is that PIV is a non-intrusive technique that can measure the instantaneous velocity field, instead of point measurements. Furthermore, PIV provides a quantitative measurement and a visualization of the flow at the same time. In this way, PIV can provide a better understanding of the flow behaviour around an object, compared to other measurement devices such as a laser Doppler anemometer.

### C.1. Tomographic-PIV

PIV started as a 2D measurement technique in which the particles were illuminated in a thin light sheet and were recorded by a single camera. Later, this technique evolved to a 3D measurement technique that uses three or more cameras and a 3D illuminated volume to track the particles. Typically referred to as tomographic-PIV [11]. It provides the full quantification of the flow, needed to be able to completely understand the 3D flow structures. Nevertheless, tomographic-PIV has not been used within industrial wind tunnels [28]. One of the reasons for this, is the system complexity and data processing burden, because among others, camera calibration is required every time the camera is relocated [14]. The limited extent of the measurement volume is another reason for the tomographic-PIV not being applied within industrial wind tunnels.

### C.2. Robotic volumetric Particle Image Velocimetry

The advent of the Helium Filled Soap Bubbles (HFSB) as tracer particles enabled the possibility to enlarge the measurement volume because HFSB scatter on the order of  $10^4$  to  $10^5$  more light than conventional tracer particles [31]. Eventually, with the introduction of the coaxial volumetric velocimeter (CVV) by Schneiders, the earlier mentioned system complexity was also highly simplified [30]. The CVV probe consists of four cameras together with an optical fibre that transmits the laser light, that

is conically expanded through a cylindrical lens. The optical fibre is located between the cameras, in this way coaxial imaging and illumination is achieved. Consequently, no calibration is required after re-positioning the CVV probe. The components of the CVV probe are shown in figure C.2. When installing the CVV probe on a robot arm, the probe can move within a specific volume, enabling the possibility of attaining optical access to a large region. The employed robotic arm is a six degree of freedom, Universal Robots UR5 robotic arm that consists of 6 joints. The arm has a maximum reach of 85 cm radius around its base and a positional repeatability of  $\pm 0.1$  mm. The UR5 robotic arm is shown in figure C.3. The combination of the probe with the robot arm is one of the most recent innovations within the field of flow measurement techniques. This measurement technique is known as Robotic volumetric PIV.

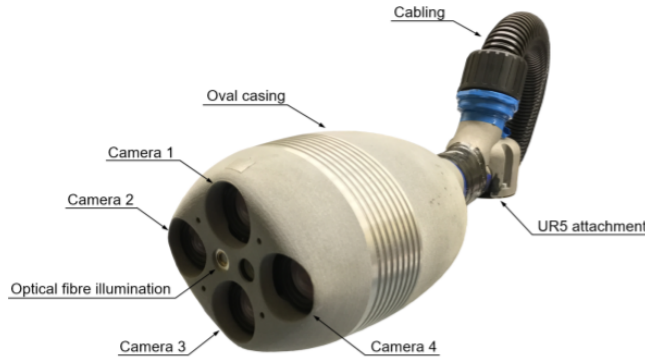


Figure C.2: The MiniShaker Aero CVV probe with the naming of the different components.

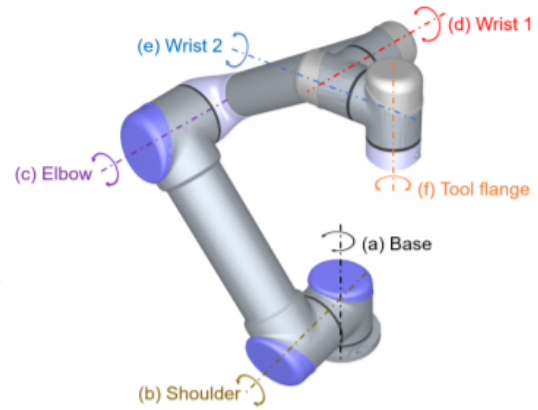


Figure C.3: The six degree of freedom Universal Robots UR5 robotic arm, including the naming of the joints.

### C.2.1. Tracer particles

Tracer particles should on the one hand be large enough to scatter a sufficient amount of light but on the other hand small enough in order to quickly adapt to the changing flow dynamics. The ability of a spherical particle to follow the flow is often expressed in terms of  $U_{slip}$  and is defined as the velocity lag of a particle in a continuously accelerating fluid. In the Stokes flow regime, the equation of  $U_{slip}$  reads as follows [24]:

$$U_{slip} = d_p^2 \frac{(\rho_p - \rho_f)}{18\mu} a \quad (C.1)$$

For which  $d_p$  is the tracer particle diameter [m],  $\rho_p$  and  $\rho_f$  the density of the particle and the surrounding fluid respectively [ $\frac{kg}{m^3}$ ],  $\mu$  the dynamic viscosity of the fluid [ $\frac{kg}{m \cdot s}$ ] and  $a$  the fluid acceleration [ $\frac{m}{s^2}$ ]. The equation only holds for small tracer particles, as it is derived from the Stokes drag, which assumes that the particle dynamics are dominated by viscous forces. Minimizing  $U_{slip}$  can either be achieved by producing small tracer particles or by producing particles with a similar density to that of the surrounding fluid. Since volumetric PIV requires particles that scatter a high level of light, minimizing  $d_p$  is not feasible. Therefore, neutrally buoyant HFSB are used. The response time of these particles is reported to be in the range of  $10\mu s$  [28].

### C.2.2. Lagrangian Particle Tracking - Shake-The-Box

Recently, a new tracking method was introduced by Schanz [29]. This Lagrangian Particle Tracking (LPT) method has significantly increased the spatial resolution while reducing the computational effort. As a result, the processing of densely seeded flows ( $\geq 0.1$  particles per pixel) is enabled. The benefit over most other tracking techniques is the fact that the LPT technique uses temporal information to predict the particle position in the subsequent image frame, by means of extrapolation of the known trajectories. The working principle of the Shake-The-Box (STB) tracking algorithm will be briefly discussed in this subsection.

First, a data set is divided into different sub-volumes. Inside these sub-volumes, no a priori particle information is available at the start of a data set. Therefore, triangulation is used in the initialization phase to find correct particle tracks. Most often, this initialization is applied to the first four frames. Particles in the consecutive image are then found based on the assumption that the particles are in close proximity, because of the small time steps between two frames.

Then, the identified particles are used to construct a first predictor that predicts the particle position in the consecutive frame. The predictor enables a reduction of the search radius, resulting in a reduced number of incorrect particle tracks. The residual image is minimized by 'shaking' the particles in space, also leading to an improvement of the predictor.

After shaking the particles, the residual image still contains untracked particles. Most likely, these particles are particles that just entered the sub-volume. These new particles are again identified by triangulation. A schematic overview of the STB working principle, retrieved from Schanz et al. [29], is shown in figure C.4. The so-called 'ghost particles', are most likely not tracked with the STB algorithm, since there is a high chance for the ghost particles to not match the predicted particle path.

Summarizing, Lagrangian STB is a computationally efficient tracking algorithm, allowing the processing of densely seeded flows. Furthermore, a high spatial resolution and a low occurrence of ghost particles are realised.

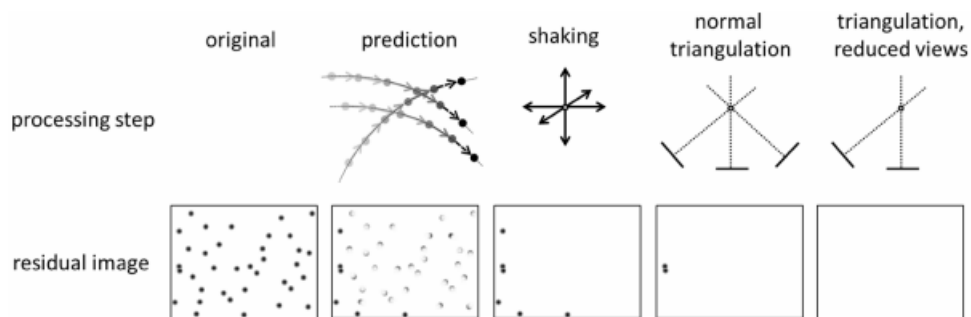


Figure C.4: Schematic overview of the working principle of the Shake-The-Box algorithm for a single time-step [29].

### C.2.3. PIV applications in sport aerodynamics

PIV has already proven to be useful to the field of sports aerodynamics. Some examples of these will be briefly illustrated in this subsection.

Hochstein et al. investigated the flow around and behind a swimmer, for underwater undulatory swimming [13]. Time-resolved 2D PIV was employed to study the flow. The focus was on vortices, created by the undulatory swimming motion and how these vortices differed from the vortices created by a subcarangiform or carangiform fish. This with the goal to eventually learn how to produce more thrust as a human swimmer. A schematic of the used set-up is shown in figure C.5.

Another example is the master thesis research of N. Mahalingesh [18]. He used large scale time-resolved stereoscopic PIV and HFSB as tracer particles to study the effect of the drafting distance and cyclist size on drag reduction. The measurements were performed using the Ring of Fire technique that enables measuring in an outdoor environment. Figure C.6 shows a schematic of the test set-up.

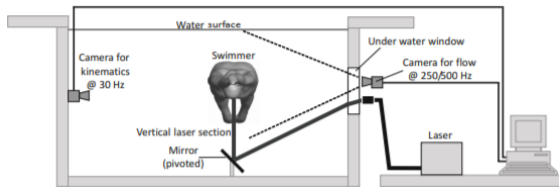


Figure C.5: Schematic of the 2D time-resolved PIV set up used to capture the flow behaviour around the undulatory swimmer [13].

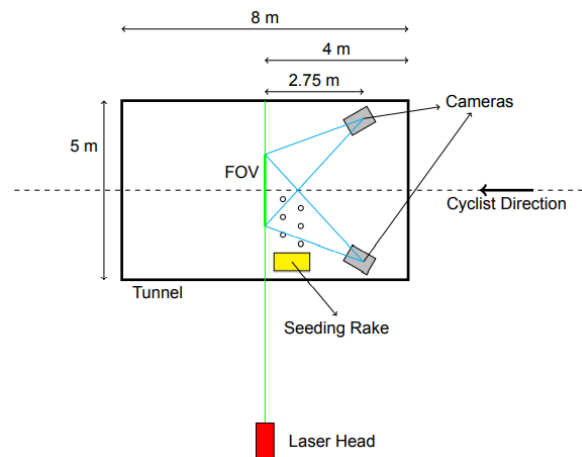


Figure C.6: Schematic of the large scale time-resolved stereoscopic PIV measurement set-up used to study the aerodynamics of on-site drafting cyclists [18].

A last example is the study performed by Jux et al., who employed Robotic PIV to determine the time-averaged properties of the velocity field developing around a full-scale time trial cyclist mannequin [14]. Figure C.7 depicts the measurement set-up that was used and figure C.8 shows the resulting time-averaged velocity field at a free-stream velocity of 14 m/s in the centre plane. This study is an example that shows the high potential of the Robotic volumetric measurement technique. The CVV probe and the robot arm together enable the optical access to a large measurement domain.

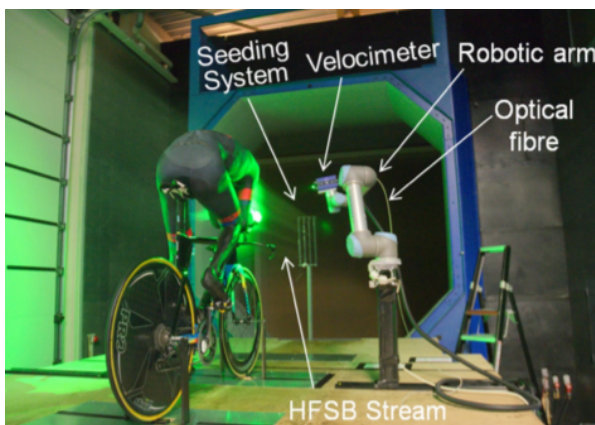


Figure C.7: The measurement set-up used by Jux et al. to determine the time averaged velocity profile of the cyclist [14].

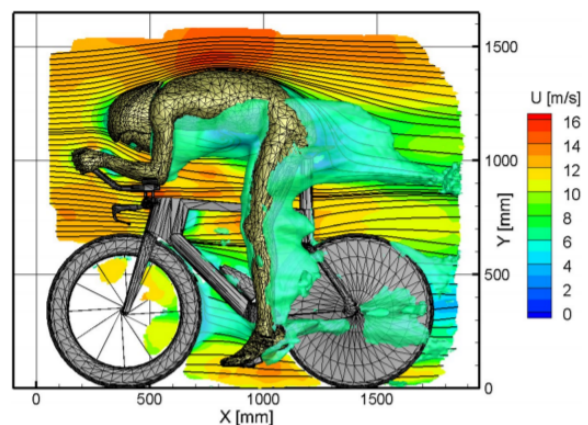


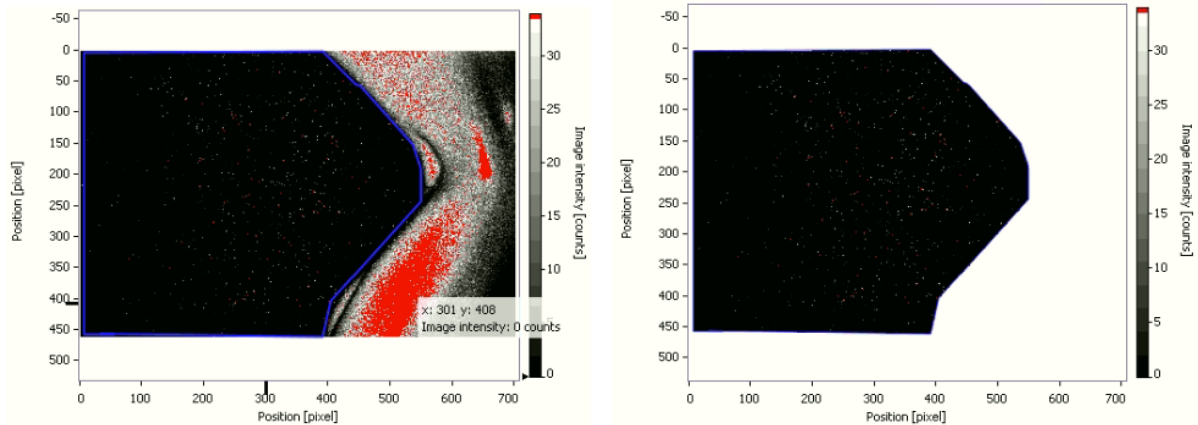
Figure C.8: The time-averaged velocity field at a free-stream velocity of 14 m/s [14].

## D. Processing operations in Davis: From raw data to binned particle tracks

This appendix illustrates the processing operations performed in Davis to get from the original recordings to the binned particle tracks.

### D.1. Masking function

First, a masking is applied to exclude the leg from the images. Not excluding the leg resulted in a high level of noise. Moreover, when the leg was included it resulted in a significant increase of the computational time. Figure D.1a shows the raw data image, figure D.1b and shows the recording after masking is applied. The area outside the blue lines in figure D.1a specifies the area that is excluded from the image. The mask function is applied for all the positions, except for the top position (position 5). For the top position, also part of the left leg is visible. The left and right leg together fill a large part of the captured area, so applying a mask function would then have led to a small remaining area in which particles can be tracked. Therefore, to remove most of the noise of the leg, a subtract average filter is applied.



(a) Raw image with the specified area outside the blue lines that will be excluded from the image.

(b) Result after applying the mask function, with the white area indicating the excluded area.

Because of the applied masking function, a gap between the leg and the velocity field exists. This may give the impression that only a small region of reverse flow is present behind the leg and should therefore be taken into account. The effect of the masking function is most pronounced in the knee region and is illustrated at three different heights along the leg in figure D.2.

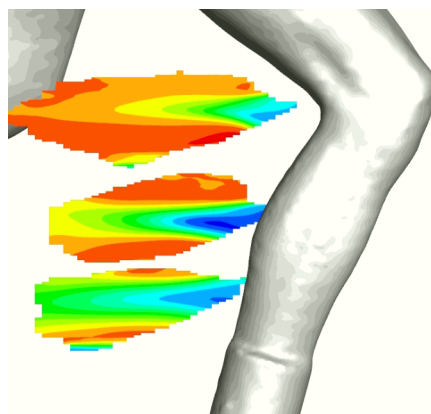


Figure D.2: Illustration of the gap between the leg and the velocity field at three different heights along the leg, caused by the applied masking function.

## D.2. Image pre-processing

Within the pre-processing operator, one can apply different type of filters to improve the image quality. The applied filters are now discussed. First, the image intensity of the raw image is scaled to a new minimum and maximum value by applying 'Subtract sliding minimum'. Then, the images are normalized, followed by a sliding Gaussian smoothing filter to remove possible noise. Hereafter, sharpening is applied to compensate for the blurring effect caused by the Gaussian smoothing. Lastly, a constant value is subtracted from each pixel and thereafter multiplied by a constant factor of 10. Figure D.3a and D.3b show the image before and after applying these filters. It can be seen that the particles are brighter, larger and look more like cross shapes after filtering.

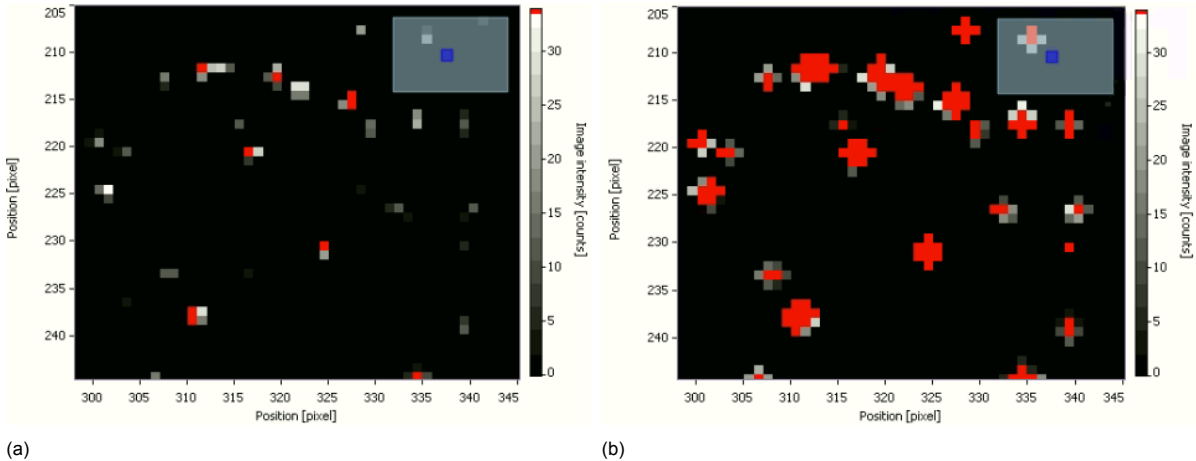


Figure D.3: Close-up of particles before (a) and after (b) the image pre-processing is applied.

## D.3. Shake-The-Box

Finally, the 'Shake-The-Box double frame with predictor' algorithm is used. The STB algorithm enables tracking of the particles in the specified measurement domain as discussed in appendix C.2.2. Within the STB operator, one can modify multiple settings to improve the quality of the particle tracks visualization. Figure D.4 shows most of the selected STB settings and figure D.5 depicts the resulting particle track visualization.

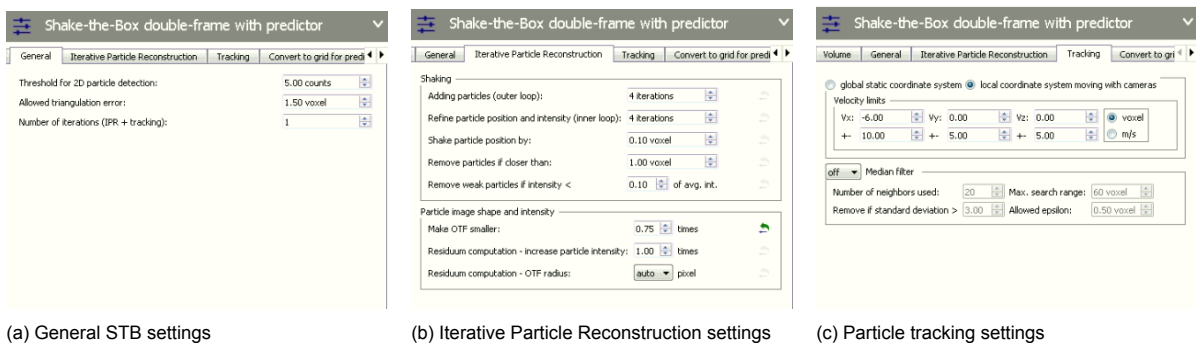


Figure D.4: Display of the settings used for the STB double-frame with predictor operator.

## D.4. Merging and binning of the particle tracks

After the image processing, the recordings of the different positions are merged. Then, binning of the particle tracks is required to be able to analyze the data in Matlab and Tecplot. A bin size of 56 voxels and 75% overlap is chosen. The minimum number of particles inside a bin is set at 20 and the spatial polynomial order is equal to zero. Bins with less than 20 particles are not shown in the visualization. With 56 voxels, the bin size is in the order of a few centimetres. This size is small enough to avoid large

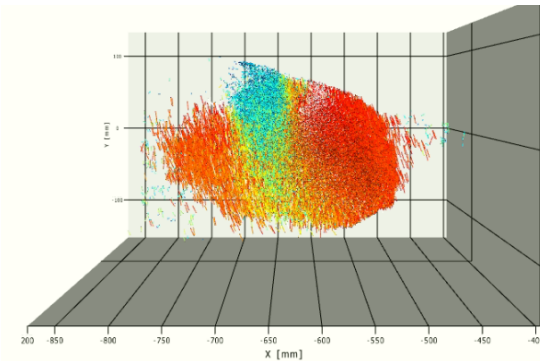


Figure D.5: Example of the particle track visualization in Davis.

spatial variations of velocity but large enough to capture at least 20 particles inside a bin, required to compute a reliable average velocity.

## E. Possible time saving

The possible time saving that can be achieved with respect to the dressed leg at 15 m/s is determined. The latter is determined based on the possible wake width reduction of 20% of the lower leg and part of the upper leg, discussed in section 4.3.4. At 15 m/s, the  $C_D A$  of the dressed mannequin is 0.23 and is obtained from figure 4.1. The lap time of a skater skating at a speed of 15 m/s is equal to 26.7 seconds. The following assumptions are made:

- Air density ( $\rho$ ) = 1.225 kg/m<sup>3</sup>
- $g = 9.81 \text{ m/s}^2$
- $\mu_{ice} = 0.003$  [33]
- Weight of skater: 80 kg

The required power output is determined using equation E.1, resulting in a power of  $\sim 510 \text{ W}$  when skating at a pace of 15 m/s.

$$P = \frac{1}{2} \rho v^3 C_d A + \mu m g v \quad (\text{E.1})$$

A new value for  $C_D A$ , corresponding to the wake width reduction of 20%, is determined using equation E.2 [32]. Similar to the work of Terra et al. (2020) an  $\alpha_d$  of  $\sim 2.0$  is assumed. It should be noted, though, that in practice  $\alpha_d$  is somewhat smaller because of the reduced difference in  $C_D$  between the sub-critical and critical regime for a roughened surface. Using equation E.2,  $C_{D A_{new}}$  is equal to  $0.4 \cdot C_D A$ .

$$\frac{C_{D,1}}{C_{D,2}} = \alpha_d \frac{d_{w,1}}{d_{w,2}} \quad (\text{E.2})$$

It is assumed that the part of the body for which the wake width reduction is obtained counts up to  $\sim 20\%$  of the complete  $C_D A$  of the skater [22] and that this reduction is obtained for 75% of the time. The latter is based on the observations that while skating, approximately 75% of the time one of the lower legs is perpendicular to the flow. Combining these assumptions with the results from equation E.2, it results in a  $C_{D A_{new}}$  of  $\sim 0.21$ .

With an average  $C_{D A_{new}}$  of 0.21, while producing a power output  $\sim 510 \text{ W}$ , a speed of  $\sim 15.5 \text{ m/s}$  is attained. This results in a lap time of 25.8 seconds, similar to a time reduction of  $\sim 0.85$  seconds per lap.

## References

- [1] Optris Infrared Measurements. <https://www.optris.global/thermal-imager-optris-pi-640>. Online; accessed 04-12-2020.
- [2] Universal Robots. <https://www.universal-robots.com/nl/producten/>. Online; accessed 04-12-2020.
- [3] E. Achenbach. Distribution of local pressure and skin friction around a circular cylinder in cross-flow up to  $re = 5 \times 10^6$ . *Journal of Fluid Mechanics*, 34(4):625–639, December 1968. doi: 10.1017/s0022112068002120. URL <https://doi.org/10.1017/s0022112068002120>.
- [4] E. Achenbach. Influence of surface roughness on the cross-flow around a circular cylinder. *Journal of Fluid Mechanics*, 46(2):321–335, March 1971. doi: 10.1017/s0022112071000569. URL <https://doi.org/10.1017/s0022112071000569>.
- [5] L.M. Bardal and R. Reid. Testing of fabrics for use in alpine ski competition suits. *Procedia Engineering*, 34:44–49, 2012. doi: 10.1016/j.proeng.2012.04.009. URL <https://doi.org/10.1016/j.proeng.2012.04.009>.
- [6] Len Brownlie, Chester Kyle, Jorge Carbo, Nate Demarest, Edward Harber, Richard MacDonald, and Matt Nordstrom. Streamlining the time trial apparel of cyclists: The nike swift spin project. *Sports Technology*, 2(1-2):53–60, January 2009. doi: 10.1080/19346182.2009.9648499. URL <https://doi.org/10.1080/19346182.2009.9648499>.
- [7] MAAHK Chowdhury. *Aerodynamics of sports fabrics and garments*. PhD dissertation, RMIT University, Melbourne, Australia, 2012.
- [8] George Constantinescu and Kyle Squires. Numerical investigations of flow over a sphere in the subcritical and supercritical regimes. *Physics of Fluids*, 16(5):1449–1466, May 2004. doi: 10.1063/1.1688325. URL <https://doi.org/10.1063/1.1688325>.
- [9] A. D’Auteuil, G.L. Larose, and S.J. Zan. Relevance of similitude parameters for drag reduction in sport aerodynamics. *Procedia Engineering*, 2(2):2393–2398, June 2010. doi: 10.1016/j.proeng.2010.04.005. URL <https://doi.org/10.1016/j.proeng.2010.04.005>.
- [10] Annick D’Auteuil, Guy L. Larose, and Steve J. Zan. Wind turbulence in speed skating: Measurement, simulation and its effect on aerodynamic drag. *Journal of Wind Engineering and Industrial Aerodynamics*, 104-106:585–593, May 2012. doi: 10.1016/j.jweia.2012.02.002. URL <https://doi.org/10.1016/j.jweia.2012.02.002>.
- [11] G. E. Elsinga, F. Scarano, B. Wieneke, and B. W. van Oudheusden. Tomographic particle image velocimetry. *Experiments in Fluids*, 41(6):933–947, October 2006. doi: 10.1007/s00348-006-0212-z. URL <https://doi.org/10.1007/s00348-006-0212-z>.
- [12] Daniele Giaquinta. The flow topology of the ahmed body in cross-wind: An experimental investigation by means of robotic volumetric piv. Master’s thesis, Delft University of Technology, 2018. URL <https://repository.tudelft.nl/islandora/object/uuid:27b75b3f-8b4d-4977-82ee-e531fd986839>.
- [13] Stefan Hochstein, Steffen Pacholak, Christoph Brücker, and Reinhard Blickhan. Experimental and numerical investigation of the unsteady flow around a human underwater undulating swimmer. In *Nature-inspired fluid mechanics*, pages 293–308. Springer, 2012.
- [14] Constantin Jux, Andrea Sciacchitano, Jan FG Schneiders, and Fulvio Scarano. Robotic volumetric piv of a full-scale cyclist. *Experiments in Fluids*, 59(4):74, 2018.
- [15] J. Kuklova, L. Popelka, N. Souckova, and T. Vitu. Visualization of airfoil boundary layer by infrared thermography to determine influence of roughness-due-to-insect. In *Proceedings of the 2012 International Conference on Quantitative InfraRed Thermography*. QIRT Council, 2012. doi: 10.21611/qirt.2012.332. URL <https://doi.org/10.21611/qirt.2012.332>.

- [16] O. Lehmkuhl, I. Rodríguez, R. Borrell, J. Chiva, and A. Oliva. Unsteady forces on a circular cylinder at critical reynolds numbers. *Physics of Fluids*, 26(12):125110, December 2014. doi: 10.1063/1.4904415. URL <https://doi.org/10.1063/1.4904415>.
- [17] L.E.M. Lignarolo, D. Ragni, C. Krishnaswami, Q. Chen, C.J. Simão Ferreira, and G.J.W. van Bussel. Experimental analysis of the wake of a horizontal-axis wind-turbine model. *Renewable Energy*, 70:31–46, October 2014. doi: 10.1016/j.renene.2014.01.020. URL <https://doi.org/10.1016/j.renene.2014.01.020>.
- [18] N Mahalingesh. On-site drafting aerodynamics of cyclists using the ring of fire. Master's thesis, Delft University of Technology, 2020. URL <https://repository.tudelft.nl/islandora/object/uuid%3A5014d292-0ed5-41de-967f-e425b3d92a08?collection=education>.
- [19] Nikhil Mahalingesh. Effect of Seeding Rake on Flow Uniformity and Turbulence Intensity of the W-Tunnel. Private communication.
- [20] Kazuyoshi Matsuzaki, Mitsuru Shingai, Yasutake Haramoto, Mizue Munekata, and Hideki Ohba. Visualization of three-dimensional flow structures in the wake of an inclined circular cylinder. *Journal of Visualization*, 7(4):309–316, 2004.
- [21] Youngjin Moon, Jooho Song, Kybeom Kwon, Ogyeong Kwon, Mikyung Kim, Seok-Han Yoon, Byun Yunghwan, and A-Na Sa. Development of a functional speed skating uniform through aerodynamic analysis on knit textiles and uniforms. *Journal of Engineered Fibers and Fabrics*, 11(4):155892501601100, December 2016. doi: 10.1177/155892501601100409. URL <https://doi.org/10.1177/155892501601100409>.
- [22] Luca Oggiano and Lars Roar Sætran. Experimental analysis on parameters affecting drag force on speed skaters. *Sports Technology*, 3(4):223–234, November 2010. doi: 10.1080/19346182.2012.663532. URL <https://doi.org/10.1080/19346182.2012.663532>.
- [23] Luca Oggiano, Olga Troynikov, Inna Konopov, Aleksandar Subic, and Firoz Alam. Aerodynamic behaviour of single sport jersey fabrics with different roughness and cover factors. *Sports Engineering*, 12(1):1–12, November 2009. doi: 10.1007/s12283-009-0029-0. URL <https://doi.org/10.1007/s12283-009-0029-0>.
- [24] Markus Raffel, Christian E Willert, Fulvio Scarano, Christian J Kähler, Steve T Wereley, and Jürgen Kompenhans. *Particle image velocimetry: a practical guide*. Springer, 2018.
- [25] Lars Sætran and Luca Oggiano. Skin suit aerodynamics in speed skating. In *Sport Aerodynamics*, pages 93–105. Springer Vienna, 2008. doi: 10.1007/978-3-211-89297-8\_5. URL [https://doi.org/10.1007/978-3-211-89297-8\\_5](https://doi.org/10.1007/978-3-211-89297-8_5).
- [26] Edoardo Saredi, Andrea Sciacchitano, and Fulvio Scarano. Multi- $\delta t$  3d-ptv based on reynolds decomposition. *Measurement Science and Technology*, 2020.
- [27] F. Scarano. Experimental aerodynamics. Unpublished course reader for the students of Flow Measurement Techniques, Delft University of technology, feb 2013.
- [28] Fulvio Scarano, Sina Ghaemi, Giuseppe Carlo Alp Caridi, Johannes Bosbach, Uwe Dierksheide, and Andrea Sciacchitano. On the use of helium-filled soap bubbles for large-scale tomographic PIV in wind tunnel experiments. *Experiments in Fluids*, 56(2), February 2015. doi: 10.1007/s00348-015-1909-7. URL <https://doi.org/10.1007/s00348-015-1909-7>.
- [29] Daniel Schanz, Sebastian Gesemann, and Andreas Schröder. Shake-the-box: Lagrangian particle tracking at high particle image densities. *Experiments in Fluids*, 57(5), April 2016. doi: 10.1007/s00348-016-2157-1. URL <https://doi.org/10.1007/s00348-016-2157-1>.
- [30] Jan F G Schneiders, Fulvio Scarano, Constantin Jux, and Andrea Sciacchitano. Coaxial volumetric velocimetry. *Measurement Science and Technology*, 29(6):065201, apr 2018. doi: 10.1088/1361-6501/aab07d. URL <https://doi.org/10.1088%2F1361-6501%2Faab07d>.

- [31] J.F.G. Schneiders. *Bridging PIV spatial and temporal resolution using governing equations and development of the coaxial volumetric velocimeter*. PhD thesis, 2017. URL <http://resolver.tudelft.nl/uuid:244b9699-0814-4bc9-aa48-07361989bd64>.
- [32] W. Terra, A. Sciacchitano, and F. Scarano. Cyclist reynolds number effects and drag crisis distribution. *Journal of Wind Engineering and Industrial Aerodynamics*, 200:104143, May 2020. doi: 10.1016/j.jweia.2020.104143. URL <https://doi.org/10.1016/j.jweia.2020.104143>.
- [33] Gerrit Jan van Ingen Schenau. The influence of air friction in speed skating. *Journal of Biomechanics*, 15(6):449–458, 1982.
- [34] Ran Wang, Shaohong Cheng, and David S-K. Ting. Effect of yaw angle on flow structure and cross-flow force around a circular cylinder. *Physics of Fluids*, 31(1):014107, January 2019. doi: 10.1063/1.5079750. URL <https://doi.org/10.1063/1.5079750>.
- [35] T. Zhou, S. F. Mohd. Razali, Y. Zhou, L. P. Chua, and L. Cheng. Dependence of the wake on inclination of a stationary cylinder. *Experiments in Fluids*, 46(6):1125–1138, February 2009. doi: 10.1007/s00348-009-0625-6. URL <https://doi.org/10.1007/s00348-009-0625-6>.